

**A THESIS SUBMITTED TO  
THE GRADUATE SCHOOL OF NATURAL AND APPLIED SCIENCES  
OF ÇANKIRI KARATEKİN UNIVERSITY**

**PERFORMANCE OF SnS: Ag DOPED Cu PREPARED BY PLD  
TECHNIQUE FOR SOLAR CELL APPLICATION**

**IN PARTIAL FULFILLMENT OF THE REQUIREMENTS  
FOR  
THE DEGREE OF MASTER OF SCIENCE  
IN  
PHYSICS**

**BY**

**AMEIRA ABDULLAH KAREIM ALMAULA**

**ÇANKIRI**

**2023**

PERFORMANCE OF SnS: Ag DOPED Cu PREPARED BY PLD TECHNIQUE FOR  
SOLAR CELL APPLICATION

By Ameira Abdullah Kareim ALMAULA

January 2023

We certify that we have read this thesis and that in our opinion it is fully adequate, in scope and in quality, as a thesis for the degree of Master of Science

**Advisor** : Prof. Dr. Çiğdem YÜKSEKTEPE ATAOL

**Co-Advisor** : Prof. Dr. Ghuson Hameed MOHAMMED

**Examining Committee Members:**

**Chairman** : Prof. Dr. Çiğdem YÜKSEKTEPE ATAOL  
Physics  
Çankırı Karatekin University

**Member** : Prof. Dr. Sebahaddin ALPTEKİN  
Physics  
Çankırı Karatekin University

**Member** : Assoc. Prof. Dr. Sibel DEMİR KANMAZALP  
Electronic and Automation, Biomedical Device Technology  
Gaziantep University

**Approved for the Graduate School of Natural and Applied Sciences**

**Prof. Dr. İbrahim ÇİFTÇİ**  
**Director of Graduate School**

**I hereby declare that all information in this document has been obtained and presented in accordance with academic rules and ethical conduct. I also declare that, as required by these rules and conduct, I have fully cited and referenced all material and results that are not original to this work.**

**Ameira Abdullah Kareim ALMAULA**

## ABSTRACT

### PERFORMANCE OF SnS: Ag DOPED Cu PREPARED BY PLD TECHNIQUE FOR SOLAR CELL APPLICATION

Ameira Abdullah Kareim ALMAULA

Master of Science in Physics

Advisor: Prof. Dr. Çiğdem YÜKSEKTEPE ATAOL

Co-Advisor: Prof. Dr. Ghuson Hameed MOHAMMED

January 2023

In this thesis, (SnS: Ag): Cu/Si solar cell was fabricated by modifying specific properties of SnS films deposited on Si wafers using the PLD technique by doping SnS: Ag with Cu at different ratios. The effect of the Cu doping ratio on the properties of the prepared thin films was investigated with using different techniques. The XRD analysis shows the polycrystalline nature of the prepared SnS powder and broad lines for thin films as its nanocrystalline structure. Additional phases appeared corresponding to Ag and Cu at a high ratio. The crystallite size reduced from 15.4 to 12.8 nm after doping with 0.05 Cu, and increased up to 14.7 with an increasing Cu ratio to 0.15, while the lattice strain has the opposite behavior. The AFM and FTIR results show the lowest roughness at a 0.05 Cu ratio and the characteristic bands for SnS. Most bands shifted towards a higher wavenumber after doping with Ag, as well as with Cu. The optical absorbance increases for the SnS: Ag sample and more increasing with the Cu content. A red shift in the band edge with Cu doping appeared. The band gap reduced from 2.2 eV for SnS to 1.75 eV for (SnS: Ag)<sub>0.85</sub>Cu<sub>0.15</sub>. The direct current conductivity shows two activation energies reduced with metal content. Both the SnS and (SnS: Ag)<sub>0.85</sub>Cu<sub>0.15</sub> were p-type, while the three others were n-type. The I-V characteristic shows typical curves with an acceptable ideality. The optimum solar efficiency of 1.28% appeared for the (SnS: Ag)<sub>0.9</sub>Cu<sub>0.1</sub>/p-Si heterojunction.

**2023, 67 pages**

**Keywords:** Silver doped SnS, Thin films, PLD technique, Solar cell, Heterojunction

## ÖZET

# GÜNEŞ PİLİ UYGULAMASI İÇİN PLD TEKNİĞİYLE HAZIRLANAN SnS: Ag KATKILI Cu'NUN PERFORMANSI

Ameira Abdullah Kareim ALMAULA

Fizik, Yüksek Lisans

Tez Danışmanı: Prof. Dr. Çiğdem YÜKSEKTEPE ATAOL

Eş Danışman: Prof. Dr. Ghuson Hameed MOHAMMED

Ocak 2023

Bu tezde, (SnS: Ag): Cu/Si güneş pili, SnS: Ag ile farklı oranlarda katkılama yapılarak PLD tekniği kullanılarak Si levhalar üzerinde biriktirilen SnS filmlerinin spesifik özellikleri modifiye edilerek üretilmiştir. Hazırlanan ince filmlerin özelliklerine Cu katkı oranının etkisi farklı teknikler kullanılarak araştırılmıştır. XRD analizi, hazırlanan SnS tozunun polikristal yapısını ve nanokristal yapısı olarak ince filmler için geniş çizgileri gösterir. Ag ve Cu'ya yüksek oranda karşılık gelen ek fazlar ortaya çıkmıştır. Kristalit boyutu 0,05 Cu ile katkılamadan sonra 15,4 nm'den 12,8 nm'ye düşmüş ve Cu oranı 0,15'e yükselerek 14,7'ye yükselmiştir. AFM ve FTIR sonuçları, 0,05 Cu oranında en düşük pürüzlülüğü ve SnS için karakteristik bantları gösterir. Çoğu bant, Cu ile olduğu kadar Ag ile de katkılamadan sonra daha yüksek bir dalga sayısına doğru kaymıştır. SnS: Ag numunesi için optik soğurulma artar ve Cu içeriği ile daha da artar. Cu katkılı bant kenarında kırmızı bir kayma görülmüştür. Bant aralığı, SnS için 2,2 eV'den (SnS: Ag)<sub>0,85</sub>Cu<sub>0,15</sub> için 1,75 eV'ye düşürülmüştür. Doğru akım iletkenliği, metal içeriği ile azaltılmış iki aktivasyon enerjisini gösterir. Hem SnS hem de (SnS: Ag)<sub>0,85</sub>Cu<sub>0,15</sub> p-tipiyken, diğer üçü n-tipidir. I-V karakteristiği, kabul edilebilir bir ideallığe sahip tipik eğrileri gösterir. (SnS: Ag)<sub>0,9</sub>Cu<sub>0,1</sub>/pSi hetero bağlantı için %1,28'lik optimum güneş verimliliği ortaya çıkmıştır.

**2023, 67 sayfa**

**Anahtar Kelimeler:** Gümüş katkılı SnS, İnce filmler, PLD tekniği, Güneş pili, Hetero bağlantı

## **PREFACE AND ACKNOWLEDGEMENTS**

I would like to express my deep thanks and gratitude to God the almighty, for his uncountable blessings.

I would like to express my deep gratitude and appreciation to my supervisors Prof. Dr. Çiğdem YÜKSEKTEPE ATAOL and my second supervisor Prof. Dr. Ghuson Hameed MOHAMMED for continuous advice and their guidance throughout this work.

Thanks are to Çankırı Karatekin University, Graduate School of Natural and Applied Sciences, Physics Department, and all the staff of the department. Also, I would like to express my thanks to the University of Baghdad, College of science, department of Physics, and the staff of the thin films laboratory especially Dr. Kadhim Abd Al WAHID for providing me with the necessary facilities during this study.

I would like to express my deep gratitude and appreciation to my friends Shatha and Nidal for their help at all times. Finally, it will be unfair on my part if I don't mention the support rendered by my sister and brothers and my son for their support, prayers, encouragement, and for various kinds of assistance, and everyone who helped me one way or another during the preparation in bring out this work.

**Ameira Abdullah Kareim ALMAULA**

**Çankırı-2023**

## CONTENTS

ABSTRACT .....	i
ÖZET.....	ii
PREFACE AND ACKNOWLEDGEMENTS.....	iii
CONTENTS.....	iv
LIST OF SYMBOLS .....	vii
LIST OF ABBREVIATIONS .....	viii
LIST OF FIGURES .....	ix
LIST OF TABLES .....	xi
1. INTRODUCTION .....	1
1.1 Literature Review.....	3
2. THEORETICAL PART.....	5
2.1 Classification of Solid Materials .....	5
2.1.1 Insulators.....	5
2.1.2 Conductors .....	5
2.1.3 Semiconductors .....	6
2.2 Semiconductors Classification .....	6
2.2.1 Amorphous semiconductors .....	7
2.2.2 Crystalline semiconductors.....	7
2.3 Semiconductor composites .....	8
2.4 Doping .....	9
2.5 Thin Film .....	9
2.6 Method of Preparation Thin Film .....	10
2.6.1 Pulsed laser deposition .....	10
2.7 Optical Properties of Semiconductors.....	12
2.7.1 Optical transition .....	14
2.8 Hall Effect .....	16
2.9 Solar Cell Heterojunction.....	17
2.10 Physical and Chemical Properties of (Sn), (S), (SnS), (Ag), (Cu), and (Si)..	19
2.10.1 Tin (Sn).....	19
2.10.2 Sulfur (S).....	19

2.10.3 Tin sulfide (SnS) .....	20
2.10.4 Silicon (Si) .....	21
2.10.5 Silver (Ag) .....	22
2.10.6 Copper (Cu) .....	22
<b>3. MATERIALS AND METHODS .....</b>	<b>24</b>
3.1 Preparation of Tin Sulfide.....	25
3.2 Preparation of Pellets.....	26
3.3 Preparation of Substrates.....	26
3.3.1 Glass slides.....	27
3.3.2 Silicon substrate .....	27
3.4 Deposition Equipment .....	27
3.4.1 Nd: YAG laser source.....	28
3.4.2 The procedure of thin film deposition by PLD .....	28
3.4.3 Thickness measurement .....	29
3.5 Structural Properties .....	30
3.6 Surface Morphology .....	32
3.7 Optical Properties Measurements .....	33
3.8 Electrodes Deposition .....	34
3.9 Electrical Measurements .....	34
3.9.1 D.C. conductivity measurement .....	34
3.9.2 Hall measurements .....	35
3.10 Heterojunction Fabrication.....	36
3.11 Current-Voltage Characteristics for Heterojunction .....	37
<b>4. RESULTS AND DISCUSSION .....</b>	<b>38</b>
4.1 X-ray Diffraction Results .....	38
4.2 Atomic Force Microscopy .....	43
4.3 Fourier Transform Infrared Spectroscopy Results .....	45
4.4 Optical Properties .....	47
4.4.1 UV-visible absorbance.....	47
4.4.2 Absorption coefficient .....	48
4.4.3 Optical energy gap.....	48
4.5 Direct Current Conductivity Results .....	50

<b>4.6 Hall Effect Measurements .....</b>	<b>52</b>
<b>4.7 I-V Characteristics for Heterojunctions .....</b>	<b>53</b>
<b>5. CONCLUSIONS AND RECOMMENDATION.....</b>	<b>58</b>
<b>5.1 Conclusions .....</b>	<b>58</b>
<b>5.2 Recommendations for Future Work .....</b>	<b>59</b>
<b>REFERENCES.....</b>	<b>60</b>
<b>CURRICULUM VITAE.....</b>	<b>67</b>



## LIST OF SYMBOLS

$D$	Crystalline size
$d_{hkl}$	Inter-atomic distances
$E_g$	Energy gap
FWHM	Full width at half maximum
$h$	Planck constant
$I$	Intensity
$I_H$	Hall current
$I_m$	Current at maximum power
$I_{Sc}$	Short circuit current
$k$	Wave vector
$N_H$	Carrier's concentration
$P_m$	Maximum power
$q$	Carrier's charges
$R_H$	Hall resistance
$t$	Film thickness
$V_H$	Hall voltage
$V_m$	Voltage at maximum power
$V_{oc}$	Open circuit voltage
$\alpha$	Absorption coefficient
$\beta$	Diffraction line breadth
$\varepsilon$	Lattice strain
$\eta$	Solar cell efficiency
$\theta$	Diffraction angle
$\lambda$	Wavelength
$\mu_H$	Electrons mobility
$\sigma$	Electrical conductivity

## LIST OF ABBREVIATIONS

AFM	Atomic force microscope
CB	Conducting band
EDX	Energy dispersive x-ray spectroscopy
FTIR	Fourier transform infrared spectrometer
I-V	Current-voltage
PLD	Pulsed laser deposition
VB	Valence band
XRD	X-ray diffraction



## LIST OF FIGURES

Figure 2.1	Schematic of the energy bands in (a) Insulator, (b) Semiconductor and (c) Conductor (Chopra and Maini 2010). .....	6
Figure 2.2	Schematics of three general types of structures (a) Single Crystal, (b) Polycrystalline and (c) Amorphous (Li 2006) .....	8
Figure 2.3	Scheme of the PLD steps (a) Laser target interaction, (b) Laser plum formation and material transition and (c) Thin film deposition (Masood <i>et al.</i> 2021). .....	11
Figure 2.4	Scheme for pulsed laser deposition setup (Chrisey and Hubler 1994). ..	12
Figure 2.5	VB-CB electronic transitions types (a) Allowed direct, (b) Forbidden direct, (c) Allowed indirect, (d) Forbidden indirect (Elliott and Gibson 1975).....	15
Figure 2.6	Schematic diagram of the Hall effect (Rai 1995).....	16
Figure 2.7	I-V curve of the solar cell in dark and under illumination (Kohl 1998) .	18
Figure 2.8	Crystal structure of SnS compound (Caballero-Calero <i>et al.</i> 2021) .....	21
Figure 3.1	Flow chart of experimental work .....	24
Figure 3.2	(A) Phase diagram of Sn-S system, (B) the used furnace, (C) vacuumed ampules containing Sn+S, and (D) opening ampules after cooling. ....	25
Figure 3.3	Preparation pellet steps (A) pressing powder in a mold, (B) taking away the pellet, and (C) the final pellet.....	26
Figure 3.4	Schematic of the experimental setup for the PLD technique .....	29
Figure 3.5	Optical thickness measurement .....	30
Figure 3.6	XRD system .....	32
Figure 3.7	UV-visible absorbance spectrometer .....	33
Figure 3.8	Schemes of the three used electrodes for (a) DC conductivity, (b) Hall effect, and (c) solar cell application .....	34
Figure 3.9	Photograph for Hall measurement systems (Ecopia HMS-3000) .....	35
Figure 3.10	(a) Sample board and (b) The electric diagram for Hall measurement...	36
Figure 3.11	Schematic diagram for heterojunction assembly .....	37
Figure 3.12	Schematic diagram for the circuit of I-V characteristics measurements.	37
Figure 4.1	X-ray diffraction pattern for SnS powder .....	38
Figure 4.2	X-ray diffraction patterns of the thin films prepared by PLD technique for SnS, SnS: Ag, and Cu-doped SnS: Ag at different ratios.....	41
Figure 4.3	Variation of crystalline size and lattice strain of the thin films prepared by PLD technique for Cu-doped SnS: Ag with the Cu ratio.....	43
Figure 4.4	AFM images for the thin films of SnS, SnS: Ag and Cu-doped SnS: Ag at different Cu ratios.....	44
Figure 4.5	FTIR patterns for the SnS, SnS: Ag and doped SnS: Ag at different Cu ratios .....	46

Figure 4.6	UV-visible absorbance spectra for the thin films of SnS, SnS: Ag, and Cu-doped SnS: Ag at different Cu ratios .....	47
Figure 4.7	Absorption coefficient for the thin films prepared by PLD for Cu-doped SnS: Ag at different Cu ratios .....	48
Figure 4.8	Calculation of energy gap for the SnS, SnS: Ag, and Cu-doped SnS: Ag thin films prepared at different Cu ratios by PLD.....	49
Figure 4.9	Logarithm of DC conductivity versus the temperature inverse for SnS, and Cu-doped SnS: Ag thin films at different Cu ratios .....	51
Figure 4.10	Variation of the two activation energies with Cu ratio for Cu-doped SnS: Ag thin films.....	52
Figure 4.11	Variation of $n_H$ and $\mu_H$ for the SnS, SnS: Ag, and Cu-doped SnS: Ag thin films at different Cu ratios .....	53
Figure 4.12	I-V characteristics heterojunctions based on SnS/Si, SnS: Ag/Si, and Cu-doped SnS: Ag/Si thin films at different Cu ratios prepared by PLD .....	55
Figure 4.13	$\ln(I)$ vs. $V$ under dark for the heterojunctions based on SnS/Si, SnS: Ag/Si, and Cu-doped SnS: Ag/Si thin films at different Cu ratios .....	56

## LIST OF TABLES

Table 2.1	Some physical characteristics of Tin.....	19
Table 2.2	Physical properties of (S) at room temperature.....	20
Table 2.3	The most important properties of tin sulfide.....	21
Table 2.4	Some properties of silicon.....	22
Table 2.5	Some properties of silver.....	22
Table 2.6	Some properties of copper.....	23
Table 4.1	X-ray diffraction parameters ( $2\theta$ , FWHM, $d_{hkl}$ , D, hkl) for the SnS pellet .....	39
Table 4.2	X-ray diffraction parameters for the thin films prepared by PLD for SnS, SnS: Ag, and Cu-doped SnS: Ag at different ratios.....	41
Table 4.3	AFM parameters for the thin films prepared PLD for Cu-doped SnS: Ag at different Cu ratios.....	45
Table 4.4	FTIR bands for the thin films of SnS: Ag and Cu-doped SnS: Ag at different Cu ratios.....	46
Table 4.5	Optical energy band gap $E_g^{Opt.}$ for the SnS, SnS: Ag, and Cu-doped SnS: Ag thin films prepared at different Cu ratios by PLD.....	50
Table 4.6	Activation energies and their ranges for the SnS, and Cu-doped SnS: Ag at different Cu ratios thin films .....	51
Table 4.7	Hall effect coefficients for SnS, SnS: Ag, and Cu-doped SnS: Ag thin films at different Cu ratios prepared by the PLD technique .....	53
Table 4.8	Photovoltaic parameters for the prepared heterojunctions.....	57

## 1. INTRODUCTION

The growth of energy demand is coordinated in modern society. Renewable energy is the most practical alternative among all sources due to its wide accessibility and environmentally benign character (Farret and Simões 2006).

Despite the great technological development, especially in the solar energy sector, the search continues to use new, inexpensive materials that reduce the impact of the final cell cost. As the energy obtained concerning the energy cost is one of the significant factors of interest in the search for renewable energy sources, especially solar energy. Solar energy which harvested from a large area to provide the bulk of the electricity used because it is easily available to everyone (Eltawil *et al.* 2009).

The received energy by the earth is many times the total energy consumed by man today, as harvesting a small part of it is sufficient to meet the global energy need. Solar energy is free energy for all the world and it is distributed in a balanced way for everyone unlike fossil fuels (Pavlovic 2019). Also, the cost of distribution is considered a large additional cost, while solar energy can be used from on-site units as an isolated source of energy in small villages. Also, the uses of solar cells instead of fossil fuels leads to a reduction in greenhouse gas emissions, which increases the quality of life for people and other living organisms (Shahsavari and Akbari 2018).

Scientists and researchers have been studying semiconductors since the early 19th century, which possess unique electrical and optical properties that make them the basic structure of modern electronic technologies. Semiconductors have a high impedance to the passage of electric current at low temperatures, while their electrical conductivity increases significantly at high temperatures (Solyman *et al.* 2018).

Thin-film science is an important areas of modern technology. The term thin film is used to describe one or more layers of atoms of a substance that are less than one micron thick. Because the film layer is thin, it is deposited on various materials known as substrates,

including glass, silicon, and metal. The use of thin film is critical in a variety of industries and research in solar cells and other photovoltaic applications (Abegunde *et al.* 2019).

Tin sulfide is of interest substance for use in thin film solar cells application. This is because of the abundant and non-toxicity of its components elements, tin and sulfur. Tin sulfide direct energy bandgap has an optimal value for photovoltaic applications to harvest optimum energy from solar radiation (Leach *et al.* 2012).

Recently, the focus of advanced materials studies has been on the creation of particles with regulated size and shape using a straightforward and affordable process, which is technologically crucial for the important issues being addressed by contemporary material science (Vikraman *et al.* 2019). The selection of deposition technique is one of the crucial parameters in varying the nanoparticles behavior of the nanoparticles and so their properties (Joshi *et al.* 2018). The Pulse laser technique is a simple can be controlled to the properties of the deposited films. PLD method is an appropriate technique for the preparation of composite semiconductors which have high melting and evaporation temperatures. It is assumed as a bottom-up method that includes the construction of the deposited matter from the sputtered atoms or molecules (Rajput 2015).

Though, many previous studies were concerned with improving the conversion efficiency for photovoltaics, still more studies are needed for the investigation of alternative low-cost materials for solar cell application using simple low-cost techniques. In this work, we tried to improve the SnS/Si heterojunction efficiency by composing silver and copper ions as dopant by studying of structural, surface morphology, optical properties, and electrical properties of the pure and doped SnS thin films. This thesis consists of the following sections

**Section 1** contains a general introduction to the energy demand and solar cell application, the literature survey of the related work.

**Section 2** gives a general theoretical concept of semiconductor materials, their classification, thin films, preparation methods, focus on pulsed laser deposition technique, characterization of semiconductors, and I-V characteristics for heterojunctions and junctions.

**Section 3** includes the preparatory steps, experimental techniques for characterization and the characterization procedure.

**Section 4** contains discussions of the examination results of deposited films including the structural properties, surface morphology, optical properties and direct current conductivity. Finally the examination result of the I-V characteristics was presented.

**Section 5** consists of the conclusions of the final results and the recommendations for future work.

## 1.1 Literature Review

(Abdelrahman *et al.* 2012) studied the optical properties of SnS thin film deposited on conducting tin oxide (ITO) using the thermal evaporation technique. The study specified that the refractive index is about 1.72 within the range of 590 to 1100 nm wavelength and it is thickness independent. This study indicates the isotropic and homogeneity of the prepared SnS thin films. The energy is around 1.32 eV. The optical behavior leads makes the thin films candidate for the fabrication of a solar cell (Abdelrahman *et al.* 2012).

(Jain and Arun 2013) studied the optical properties of SnS thin films prepared by evaporation of SnS in a vacuum. Using XRD observed that the grain size increased linearly with film thickness. The energy band gap is between 1.8 to 2.1 eV reliant on the particle size and lattice parameter. The SEM images show an arrangement in layered structure (Jain and Arun 2013).

(Kumar *et al.* 2014) investigated the result of doping with Ag on the main properties of tin sulfide thin films prepared by spray pyrolysis on glass bases at 350°C temperature. The XRD analysis showed improving the crystallization with increasing the Ag ratio. The surface roughness of tin sulfide films increased after doping. The lowest value of the resistivity was  $8.63 \times 10^{-1} \Omega \cdot \text{cm}$ . The carrier's concentration increased. The energy gap was 1.33 eV at 8% of Ag. The result films are a candidate for use in photo electronic applications (Kumar *et al.* 2014).

(Vikraman *et al.* 2019) investigated the ability to tune the SnS nanostructures shape and size in thin film prepared by electrodeposition technique. The SEM confirmed the surface modification of SnS nanoparticles. Different electrodes were used to alter the size of SnS. The XRD shows the polycrystalline orthorhombic structure of the SnS. The optical energy gap was in the range of 1.23–1.26 eV. The prepared samples are a candidate for use in optoelectronic devices (Vikraman *et al.* 2019).

(Baby and Bharathi Mohan 2019) studied the structural, optical, and electrical behavior of DC-RF co-sputtered Cu, In & Ag doped SnS thin films at 400 °C substrate temperature for solar cell applications. Rising the doping level to 10% by changing the DC sputtering voltage as clear from the EDAX analysis. The XRD analysis shows increasing the doping to 5% caused  $2\theta$  to shift to a higher angle due to reducing the unit cell dimension as a result of substitutional doping, while at 10% doping inverse manner appeared. The band gap of 1.33 eV and better electrical properties appeared at 4.8% of Cu doping which could be considered a better absorber material in a thin film to enhance the solar cell efficiency (Baby and Bharathi Mohan 2019).

(Dai Nguyen *et al.* 2021) determined the outcome of embedded Ag ions in SnS using the RF sputtering as SnS/Ag/SnS triple layer films for photovoltaic applications. The solar cell increased both short circuit current from 14.21 to 17.13 mA/cm<sup>2</sup> and maximum efficiency from 3.23 to 5.24% after the embedding of the Ag layer due to boost the final efficiency of the SnS solar cell (Dai Nguyen *et al.* 2021).

## **2. THEORETICAL PART**

### **2.1 Classification of Solid Materials**

Solid materials differ from each other in the composition of energy bands, and accordingly they differ in electrical conductivity. It can be classified into three categories according to its electrical conductivity, which are insulators, conductors and semiconductors (Moharam *et al.* 2021).

#### **2.1.1 Insulators**

Its electrical conductivity is in the range ( $10^{-8}$ - $10^{-18}$   $\Omega\cdot\text{cm}^{-1}$ ), in which the electrons in the valence band are close to the atom at their levels, so the electrons need a very strong electric field to get rid of the attraction of the nucleus. In other words, insulators don't contain free carrier charges under normal condition. This type includes most organic materials. The bands of energy in them are characterized by the following (Jiles 2014):

- It has a valence band filled with electrons.
- It has a conduction band devoid of free electrons.
- It has a large energy gap, which makes no electrons transferred to the conduction band at normal temperatures, and very low conductivity at high temperatures.

#### **2.1.2 Conductors**

Its conductivity is within the range  $10^3$ - $10^{18}$   $\Omega\cdot\text{cm}^{-1}$ . Conductors are characterized by the overlap of the valence and the conduction bands, and therefore the bandgap energy disappears. The conductor materials have many free electrons, so the electric current passes quickly through them (Bird 2002).

### 2.1.3 Semiconductors

Pure semiconductors are behaving as insulators at low temperatures, but they become somewhat good electrical conductors when the temperature is raised. The energy gap is narrow so that a change in the temperature can lead to the excitation of valence electrons transfer through the forbidden energy gap to the empty conduction band. The conductivity of semiconducting materials lies between the conductivity of both insulators and conductors, i.e. between  $(10^{-8}-10^3 \text{ ohm}^{-1} \text{ cm}^{-1})$ . Semiconductor materials are affected by heat, light, and magnetic fields, in addition to the impact of impurities. Figure 2.1 shows a schematic of electronic bands in the three types of material (Bird 2002).

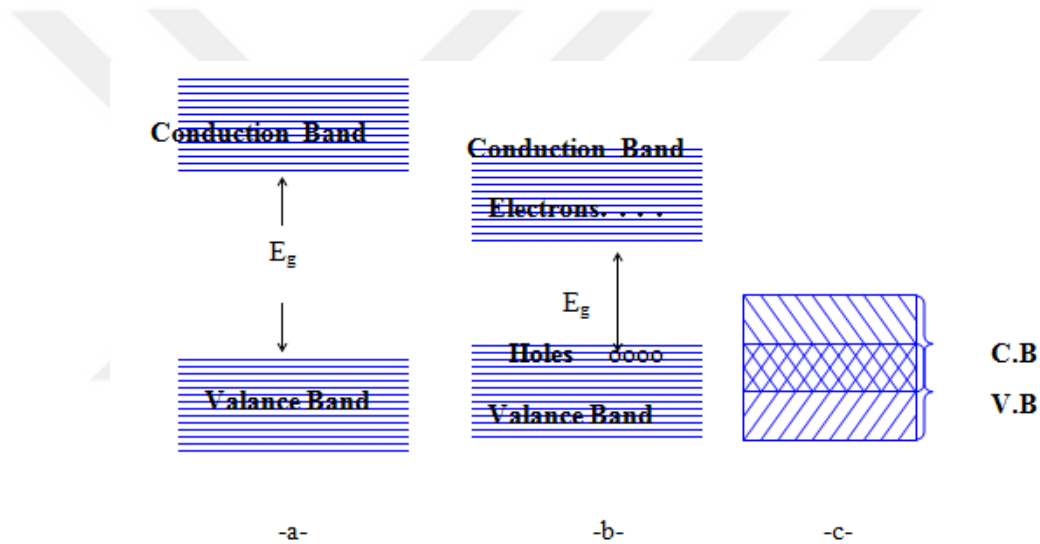


**Figure 2.1** Schematic of the energy bands in (a) Insulator, (b) Semiconductor and (c) Conductor (Chopra and Maini 2010).

## 2.2 Semiconductors Classification

The physical manner that atoms come together to form a crystalline structure determines a material's properties. Therefore, semiconductors in a crystalline solid are categorized according to the type of atom arrangement (Solymar *et al.* 2018).

### **2.2.1 Amorphous semiconductors**

In one class, the atoms are set irregularly, without long-range order in their atomic arrangement. This class of solids is commonly known as amorphous materials. These type don't have a uniform composition. They don't have a particularly specific melting point. These materials' atom arrangements aren't completely random, but they lose periodicity in three dimensions, with ordering limited to a few atomic or molecular dimensions.

### **2.2.2 Crystalline semiconductors**

In another type, the atoms are organized in systematic order. This type is usually denoted as crystalline solids. They have a uniform composition and a distinct geometrical shape. Their properties, such as refractive index, electrical conductivity, and permittivity change with direction. The crystalline solids are also separated into two groups: single crystalline and polycrystalline solids. The single crystalline solid, which have a periodicity to the lattice that extends right through the entire crystal. As a result of their high degree of order, these materials have long-range order (LRO) in three dimensions. In a polycrystalline category the regular construction only obeys over a small range of the crystal. The material is made up of many tiny single crystals called grains separated by grain boundaries. The grains in the polycrystalline state have Short Range Order (SRO) with random grain sizes, shapes, and orientations.

The distinction between these different types of solids can be achieved by using of the X-ray diffraction technique. Figure 2.2 shows a schematic of the crystalline categories (Li 2006).

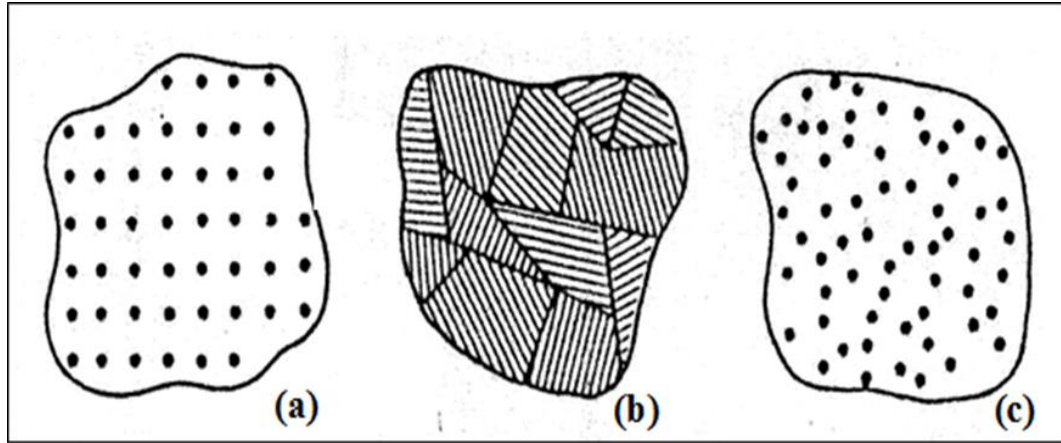


**Figure 2.2** Schematics of three general types of structures (a) Single Crystal, (b) Polycrystalline and (c) Amorphous (Li 2006)

### 2.3 Semiconductor composites

One of the oldest ways for modifying material qualities is by mixing two materials. When two semiconductors A and B are combined using a suitable growth technique, then the following characteristics are modified:

- **The lattice's crystalline structure:** In most semiconductors, if the components have the same crystal structure, resulting in the same crystalline structure in the final composites. The lattice constant of  $A_xB_{1-x}$  composite for the same lattice structure obeys Vegard's Equation (2.1).

$$a_{\text{alloy}} = xa_A + (1-x)a_B \quad (2.1)$$

- **Composites band structures:** In principle, alloy band-structures are difficult to compute because alloys are not ideal crystals, even if their lattice is flawless. This is because the atoms are arranged at random and not in any particular order. The virtual crystal approximation (VCA) provides a straightforward solution to the problem, in which the band-structure of the alloy  $A_xB_{1-x}$  is just the weighted of A and B. As a result, the bandgap can be predicted from Equation (2.2):

$$E_g^{alloy} = xE_g^A + (1-x)E_g^B \quad (2.2)$$

In most composites, however, the growing disorder causes a bowing effect. The band gap described by the relation is defined as Equation (2.3):

$$E_g^{alloy} = a + bx + Cx^2 \quad (2.3)$$

The bowing parameter is denoted by the constant C. The majority of qualities can be approximated by a linear averaging of the individual properties of the contents (Dridi *et al.* 2022).

## 2.4 Doping

Doping is the addition of impurities to intrinsic semiconductors to change their characteristics. Doping silicon and germanium were achieved using trivalent and pentavalent elements (Mondal *et al.* 2015). When a trivalent impurity is used to dope an intrinsic semiconductor, the result is a p-type semiconductor. In p-type, there are many holes or positive ions in the semiconductor, while to get n-type pentavalent elements are used. In n-type semiconductors electrons, are presently more than positiveholes (Shahid *et al.* 2016).

## 2.5 Thin Film

A thin film is a material layers that has been produced and applied on a selected substrate. It typically has a thickness of less than a micron (Zhou *et al.* 2015).

Thin films are commonly used in a variety of modern industries and are crucial bases to for technologies. They are most productively and significantly utilized in integrated circuits. A number of other industries, such as solar cell technologies and superconducting materials, also use them as crucial components. The vast array of effective applications

for thin film in research, engineering, and business is primarily due to the science's improving understanding of the nature of the processes used to deposit thin film (Perednis and Gauckler 2005).

## **2.6 Method of Preparation Thin Film**

There are two main categories of thin film deposition processes, depending on whether the deposition is physical or chemical. There is a basic difference between the two categories (Wang *et al.* 2014). Physical methods include, sputtering (Rydosz and Szkudlarek 2015), thermal evaporation (Zaien *et al.* 2013) pulsed laser deposition (Widegren and Finke 2003), and dip coating (Pileni 2006), while chemical methods include chemical vapor deposition (CVD) (Choy 2003), spray pyrolysis (Babar *et al.* 2011), sol-gel technique (Jurablu *et al.* 2015) etc.

This study used pulsed laser deposition (PLD), which is a physically easy and cheap method, to create thin semiconductor film layers (Rajput and Purohit 2016).

### **2.6.1 Pulsed laser deposition**

The fundamentals of the deposition technique play a significant role in the characteristics of the prepared thin films. PLD technology is a suitable approach for producing various semiconductors with high melting and evaporation temperatures. It is thought to be a bottom-up approach that entails building the deposited material out of sputtering atoms or moles. The deposited samples are identical chemically to the target components in their ratios (Rajput 2015).

The pulsed laser deposition composes of three stages: vaporizing the laser-assisted material, moving the plasma column containing the various species, and finally condensing the thin layer on the substrate. Using several laser pulses, these three steps are repeated several times during the deposition process. The stages of the interaction of the laser with the target material during pulse laser bombardment are depicted in Figure

2.3, with several laser pulses, the layer-by-layer process occurs in a vacuumed chamber (Barhdadi *et al.* 2012).

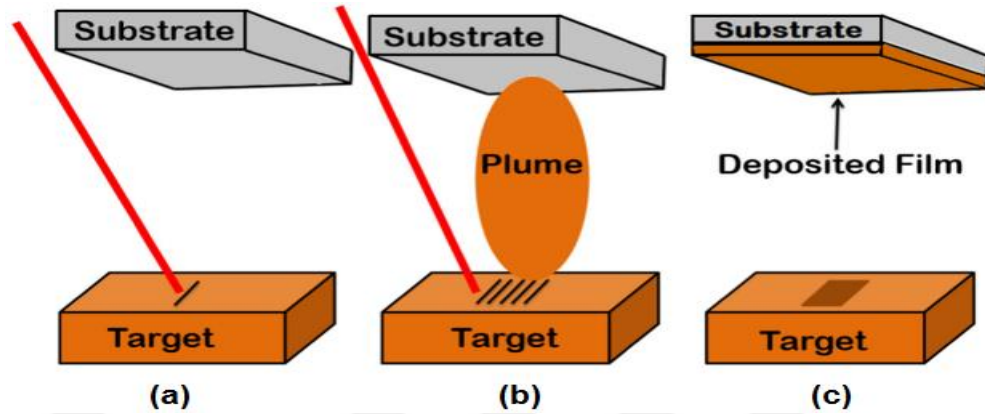


**Figure 2.3** Scheme of the PLD steps (a) Laser target interaction, (b) Laser plume formation and material transition and (c) Thin film deposition (Masood *et al.* 2021).

The PLD technique has been widely used to make create films with good specifications. This method deposits vapors into a vacuum by using physical processes. The target of the substance or a mixture is put in the focal point of the pulsed laser. A small amount of material evaporates with each laser pulse and then is transported by the plasma column to the substrates facing the target. This technique demonstrated efficiency and simplicity in creating thin films of high evaporated temperature. The target composes of the content of the mixture. Figure 2.4 shows a diagram for the PLD technique (Eason 2006).

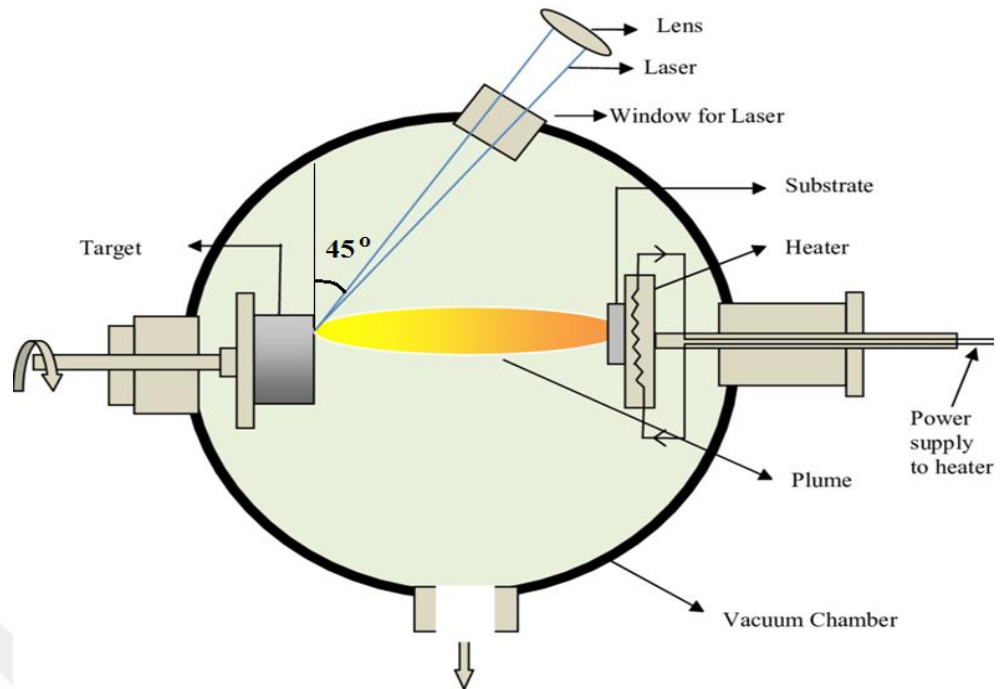


**Figure 2.4** Scheme for pulsed laser deposition setup (Chrisey and Hubler 1994).

The benefits of the PLD technique can be summed up as follows (Lin 2009):

- Crystalline films can be created at room temperature for substrates that do not withstand high temperatures.
- The laser source is placed outside the chamber, so high-purity films can be prepared.
- It is simply used to deposit a complex mixture of materials.
- The materials with high evaporation points can be deposited.
- Thin films can be prepared with the presence of certain gases.
- The targets used are small in size compared to other sputtering techniques.

## 2.7 Optical Properties of Semiconductors

Studying the optical properties is an important investigation, which allows identifying the type and value of the forbidden energy gap ( $E_g^{Opt}$ ) as well as studying the transmittance, absorption, reflectivity, and optical constants.

The optical characteristics depend on the shape of the bands and the value of the energy bands separation, which is the energy separation between the valence band (VB) and the conduction band (CB) forbidden to exist electrons. As a result of the falling photons' interactions with the material's electrons, some energy is removed from the incoming radiation. The main interaction occurs between the electric field accompanying the electromagnetic rays and the charges in the material. If the photon energy is greater or equal to the energy gap ( $h\nu \geq E_g^{Opt}$ ) where  $\nu$  is frequency, this energy is sufficient to create an electron-hole pair in the semiconductor. Meaning that the electron will cross the forbidden energy gap ( $E_g^{Opt}$ ) to the electronic conduction band when the light frequency is equal to a specific value called a critical frequency ( $\nu_o$ ) and the material will absorb part of the incident radiation. The critical frequency can be determined according to the relation, Equation (2.4) (Dresselhaus and Thomas 2001):

$$h\nu_o = E_g^{Opt}. \quad (2.4)$$

This is called the basic absorption edge of the material, and the absorption edge sharpness depends on the crystalline degree of semiconductors. The photon energy depends on its wavelength as shown by Equation (2.5) (Greiner and Eggers 1989):

$$h\nu = \frac{hc}{\lambda} \text{ or } h\nu [eV] = \frac{1240}{\lambda [nm]} \quad (2.5)$$

An important optical constant that determines the optical identity of each material is the absorption coefficient ( $\alpha$ ), which represents the decrease in the intensity of light rays falling on the material per unit thickness. The absorption coefficient depends on the energy of the incident photons, the wavelength, the surface nature, the semiconductor energy bandgap and the type of transitions between electronic levels of energy bands. The intensity of the light transmitted through the semiconductor films reduce according to  $\alpha$  as shown by Beer-Lambert Equation (2.6) (Neamen 2003):

$$I = I_o \exp(-\alpha t) \quad (2.6)$$

Where ( $t$ ) represents the thickness of the material, which ( $I_0$ ) is the incident light intensity, ( $I$ ) is the transmitted intensity. Also, Equation (2.7) can be written as follows:

$$\alpha = 2.303 A/t \quad (2.7)$$

Where  $A$  is the absorbance; there are two basic types of valence-to-conduction bands electronic transition in semiconductors, direct and indirect, each of which is divided into allowed and forbidden types. These transitions are implicated in the photons-electron interaction at the valence band to create electron-hole pairs (Adler 1971).

### 2.7.1 Optical transition

The type of valence-to-conduction bands electronic transition is subjected according to Tauc's relation Equation (2.8) (Adler 1971).

$$\alpha h\nu = B (h\nu - E_g)^r \quad (2.8)$$

Where  $B$  is an amorphousness-inverse constant,  $r$  is the exponent factor depending on the type of transition,  $h\nu$  is the photon energy, and  $E_g^{opt}$  is the energy band gap. The  $r$  value takes the values  $1/2$ ,  $3/2$ ,  $2$  and  $3$  for the direct allowed, direct forbidden, indirect allowed and indirect forbidden transitions, respectively.

The direct transition takes place between the highest point in the valence band and the lowest point of the conduction band (vertical transition), i.e. the momentum difference between the two states is equal to zero ( $\Delta k=0$ ). For allowed direct transition the wave vector for the initial and final state is equal to zero ( $k=0$ ) as seen in Figure 2.5 (a). This type of transition occurs in both crystalline and polycrystalline semiconductors, while the transition is called forbidden direct transition if it happens between states of the same wave vector but the wave vector does not equal zero, as shown in Figure 2.5 (b) (Mott and Davis 2012).

In an indirect transition, there is a considerable momentum difference between the electron state in the valence and conduction bands ( $\Delta k \neq 0$ ). This indicates that the conduction band minima differ from the valence band maxima in  $k$ . As a result, the help of a phonon is required (crystal vibration) to conserve momentum, as follows in Equation (2.9) (Greiner 1961):

$$h\nu = E_g \pm E_p \quad (2.9)$$

$E_p$  represents the energy of a phonon that has been absorbed or emitted

The allowed indirect transitions occur from the maximum point of the V.B. at ( $k=0$ ) to any point in the conductive band, as exposed in Figure 2.5 (c), while the forbidden disallowed indirect transitions occur from any location near the top of the valence band to any point other than the bottom of the conduction band, as shown in Figure 2.5 (d) (Kazmerski 1980). The absorption coefficient ( $\alpha$ ) varies from  $10^4$  to  $10^5 \text{ cm}^{-1}$  for direct bandgap and  $10$  to  $10^3 \text{ cm}^{-1}$  for indirect ones at the absorption edge, thus it can be used to distinguish between direct and indirect transitions experimentally.

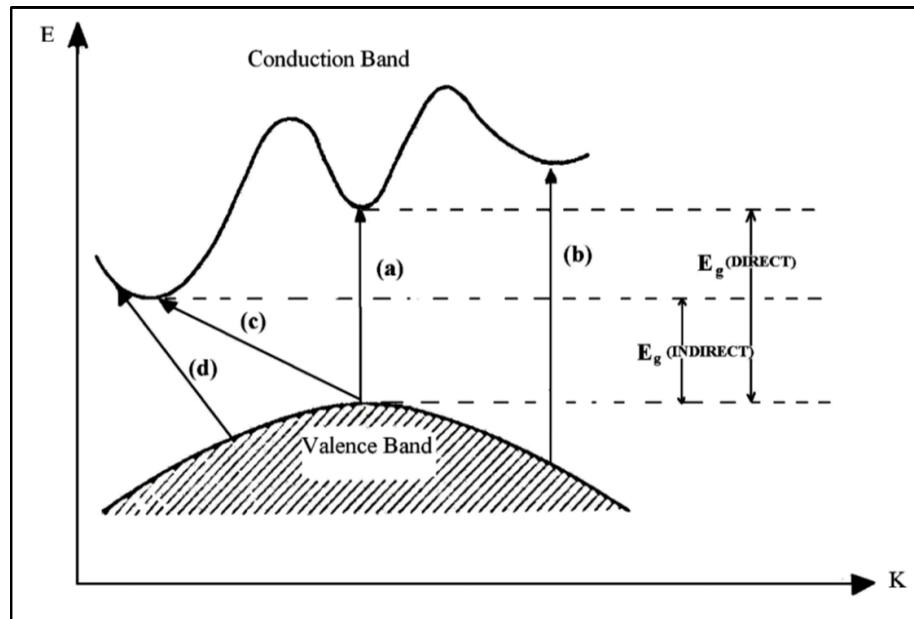


**Figure 2.5** VB-CB electronic transitions types (a) Allowed direct, (b) Forbidden direct, (c) Allowed indirect, (d) Forbidden indirect (Elliott and Gibson 1975).

## 2.8 Hall Effect

Since Edwin Hall discovered the phenomena in 1879, Hall effect measurements have been useful tools for material characterization (Hall 1879). When a current flows through a sample and a magnetic field perpendicular to the current, a Lorentz force exerts to the charge induced on the particle, which in turn produces a transverse voltage that is perpendicular to both the magnetic field and the current (Figure 2.6) (Rai and Raj 2004).

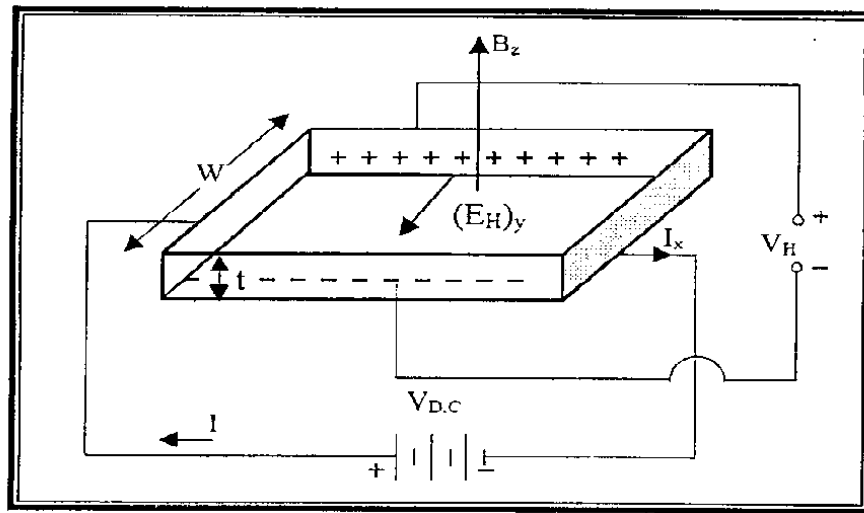


**Figure 2.6** Schematic diagram of the Hall effect (Rai 1995)

One of the most important techniques for examining the electrical characteristics of semiconductors is the Hall Effect, which provides data on the nature, abundance, and mobility of the majority of charge carriers. Hall effect coefficient ( $R_H$ ) is proportional to the induced potential divided by the applied magnetic field. The Hall coefficient ( $R_H$ ) is determined using Equation (2.10) (Rai 1995):

$$R_H = \frac{V_H}{I} \cdot \frac{t}{B} \quad (2.10)$$

Where  $t$  is the sample thickness, the term  $(\frac{V_H}{I})$  represents the slope of the linear relation between the  $V_H$  and the output current  $I$ , while  $B$  is the strength of the applied magnetic

field. The  $R_H$  sign is in the above Equation (2.11) according to the type of semiconductor so it is negative for a n-type semiconductor and positive for a p-type semiconductor.

The charge carrier concentration ( $n_H$ ) is calculated using the Hall coefficient according to the relation (Lindberg 1952):

$$n_H = \frac{1}{|R_H|.e} \quad (2.11)$$

While mobility  $\mu_H$  is calculated using both conductivity ( $\sigma$ ) and  $R_H$  Equation (2.12)

$$\mu_H = \sigma |R_H| \quad (2.12)$$

## 2.9 Solar Cell Heterojunction

The p-n junction is the basis for diodes, transistors, solar cells, and other devices. A p-n junction forms at the boundary between n-type and p-type semiconductors.

The I-V curve characteristic for heterojunctions is the superposition of its I-V curve in dark case due to the light-generated current. The light is shifted from the IV curve downward into the fourth quadrant where power can be extracted. The Equation (2.13) for the I-V curve under light is (Kohl 1998):

$$I_F = I_s \left[ \exp\left(\frac{qV}{\beta K_B T}\right) - 1 \right] \quad (2.13)$$

$I_F$  represent the forward current, and  $I_s$  is the saturation current, and  $\beta$  is the ideality factor. The -1 term in the above Equation (2.14) can usually be neglected. The exponential term is usually  $\gg 1$  at low voltages.

$$I_F = I_s \exp\left(\frac{qV}{\beta K_B T}\right) \quad (2.14)$$

The power curve has a maximum point where the solar cell should be operated to give the maximum power output, and occurs at a voltage of  $V_M$  and a current of  $I_M$ . The other parameters used to characterize solar cells such as the short-circuit current ( $I_{SC}$ ), and the open-circuit voltage ( $V_{OC}$ ) are shown in Figure 2.7 (Lindholm *et al.* 1979).

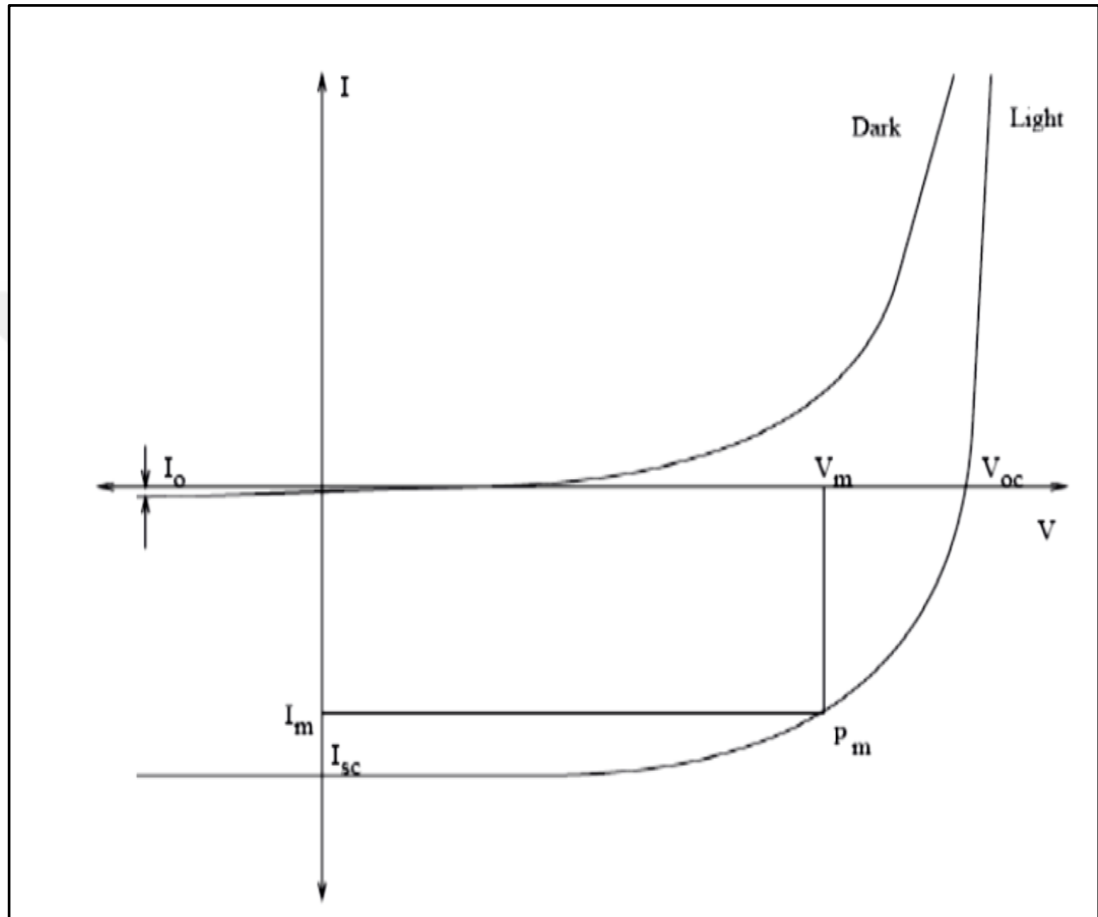


**Figure 2.7** I-V curve of the solar cell in dark and under illumination (Kohl 1998)

Another important parameter for solar cells, which determine their quality, is the fill factor ( $FF$ ). This is the maximum power ( $P_m$ ) divided by the open circuit voltage ( $V_{oc}$ ) and the short circuit current ( $I_{sc}$ ), Equation (2.15):

$$FF = \frac{P_m}{I_{sc}V_{oc}} \quad (2.15)$$

Photovoltaic efficiency measures the percentage of light power ( $P_{in}$ ) that can be converted into electrical power, Equation (2.16):

$$\eta = \frac{P_m}{P_{in}} = \frac{FF \cdot I_{Sc} \cdot V_{oc}}{P_{in}} \quad (2.16)$$

## 2.10 Physical and Chemical Properties of (Sn), (S), (SnS), (Ag), (Cu), and (Si)

Some properties of the material used in our study are given below.

### 2.10.1 Tin (Sn)

Tin is a highly crystalline, and silver color metal. Tin crystals are the first materials to exhibit the superconductors conductance properties. Tin can be highly polished and used as a protective coating for other metals, although it is susceptible to attack from acids and alkalis and does not withstand corrosion from water. Table 2.1 lists some of the Sn physical characteristics (Meskers 2021).

**Table 2.1** Some physical characteristics of Tin

Factor	Specific
Form	Solid
Crystalline structure	Tetragonal
Mass density	5.769 (g/cm <sup>3</sup> )
Melting temperature	231.9 (°C)
Boiling temperature	2602 (°C)
Atomic mass	118.7 (g/mol)

### 2.10.2 Sulfur (S)

Sulfur is well-known since ancient times, it can be found near volcanic vents. Solid sulfur is soft, pale yellow, flavorless, and brittle. It is soluble in carbon disulfide but insoluble in water. Both crystalline and amorphous allotropes of sulfur exist. Sulfur is also an

essential element for all life. Table 2.2 lists a some of the (S) element's physical characteristics (Tebbe *et al.* 1982):

**Table 2.2** Physical properties of (S) at room temperature

Factor	Specific
Form	Solid
Crystalline structure	Orthorhombic
Mass Density	2.070 (g/cm <sup>3</sup> )
Melting temperature	115.2 (°C)
Boiling temperature	444.70 (°C)
Atomic mass	32.06 (g/mol)

### 2.10.3 Tin sulfide (SnS)

Tin Sulfide (SnS) is a semiconductor from the IV-VI group, with a bandgap of  $E_g=1.30$  eV. It is crystalline as an orthorhombic structure of lattice constants a, b, and c equal 4.239, 11.193, and 3.984 Å, respectively, as presented in Figure 2.7. It may have revealed the p-type conductivity and n-type conductivity according to the content of tin and sulfide as well as changed its the type of conduction from p to n type according to treatment temperature, which can be applied in n-p homojunction and heterojunction. Table 2.3 gives some physical properties of SnS film.

Tin sulfide thin films have gained a lot of interest due to their intermediate energy band gap and high fundamental absorption coefficient. Due to the benign nature and abundance of the component elements Sn and S, devices that are both safe for the environment.

These films can be produced by different techniques, like plasma-enhanced chemical vapor deposition, thermal evaporation, chemical bath deposition, spray pyrolysis, and pulse laser deposition technique (PLD) as adopted in this work (Koteeswara Reddy *et al.* 2015) (Figure 2.8).

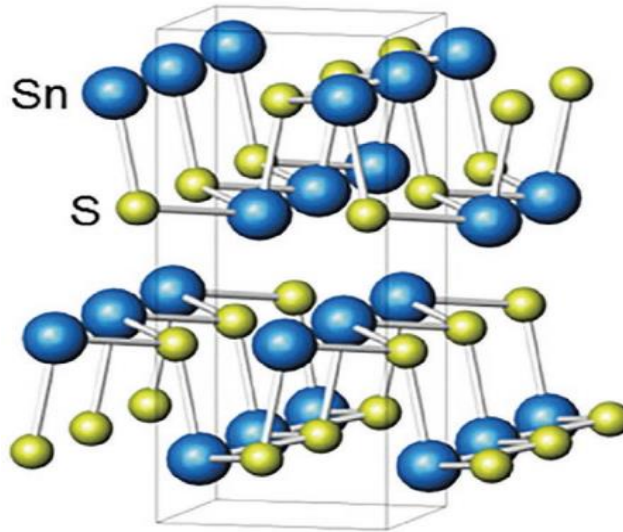


**Figure 2.8** Crystal structure of SnS compound (Caballero-Calero *et al.* 2021)

**Table 2.3** The most important properties of tin sulfide

Factor	Specific
Form	Solid
Color	Yellow
Boiling point	1230 (°C)
Crystalline structure	Orthorhombic
Mass density	5.22 (g/cm <sup>3</sup> )
Melting point	882 (°C)
Molecular Weight	150.76 (g/mol)

#### 2.10.4 Silicon (Si)

Silicon is the most abundant material in the world after oxygen. Silicon has a crystal structure known as a diamond lattice, which is a cubic crystal that can be considered as two secondary Face-Centered cubic lattices, overlapping with a quarter of the distance along the cubic side. Table 2.4 shows the properties of silicon. Single-crystal silicon is formed by crystal growth from very pure silicon along a selected crystalline direction. The required impurities are added in very small proportions to convert them to n- or p-type silicon. The process involves cutting and polishing silicon wafers for use in a variety of applications such as photovoltaic. Table 2.4 illustrates the important characteristics of silicon (Krishnan 2021).

**Table 2.4** Some properties of silicon

<b>Factor</b>	<b>Specific</b>
Melting point	1412 (°C)
Color	Gray
Bandgap energy	1.12 (eV)
Molecular weight	97.90 (gm/mole)
Refractive index	3.44
Mass density	2.34 (gm/cm <sup>3</sup> )
Crystal structure	Diamond

### 2.10.5 Silver (Ag)

Silver is an element located in Group 11 and Period 5 of the periodic table between Cu and Au, and its physical and chemical properties are intermediate between those two metals. It is a white metal of high electrical conductivity. Table 2.5 illustrates the important characteristics of silver (Krishnan 2021).

**Table 2.5** Some properties of silver

<b>Factor</b>	<b>Specific</b>
<b>Form</b>	Solid
<b>Crystalline structure</b>	Cubic
<b>Mass density</b>	10.49 (g/cm <sup>3</sup> )
<b>Melting temperature</b>	960.8 (°C)
<b>Boiling temperature</b>	2212 (°C)
<b>Oxidation states</b>	+1, +2, +3
<b>Atomic mass</b>	107.87 (g/mol)

### 2.10.6 Copper (Cu)

Copper is a chemical element with an atomic number of 29. It is a soft, malleable, and ductile metal with very high thermal and electrical conductivity. It has a red-orange color. Copper is used as a conductor of heat and electricity, as a building material, and as a constituent of various metal alloys. Their alloys are used in marine hardware and coins, and constantan is used in strain gauges and thermocouples. It is widely used in material

science as a doping element to enhance the properties of the prepared composite (Lide 2004) (Table 2.6).

**Table 2.6** Some properties of copper

<b>Factor</b>	<b>Specific</b>
<b>Form</b>	Solid
<b>Crystalline structure</b>	Cubic
<b>Mass density</b>	8.96 (g/cm <sup>3</sup> )
<b>Melting temperature</b>	1084.62 (°C)
<b>Boiling temperature</b>	2562 (°C)
<b>Oxidation states</b>	+1, +2
<b>Atomic mass</b>	63.546 (g/mol)

### 3. MATERIALS AND METHODS

This section compose the used materials, the steps of pellet pressing, substrates preparation, thin film deposition by PLD and the techniques used for the characterization of the thin films including XRD, AFM, FTIR, UV-visible absorbance, DC conductivity, and Hall effect measurements. Finally the preparation of heterojunctions based on the prepared thin films and their examination. Figure 3.1 shows the scheme for the steps of the experimental procedure.

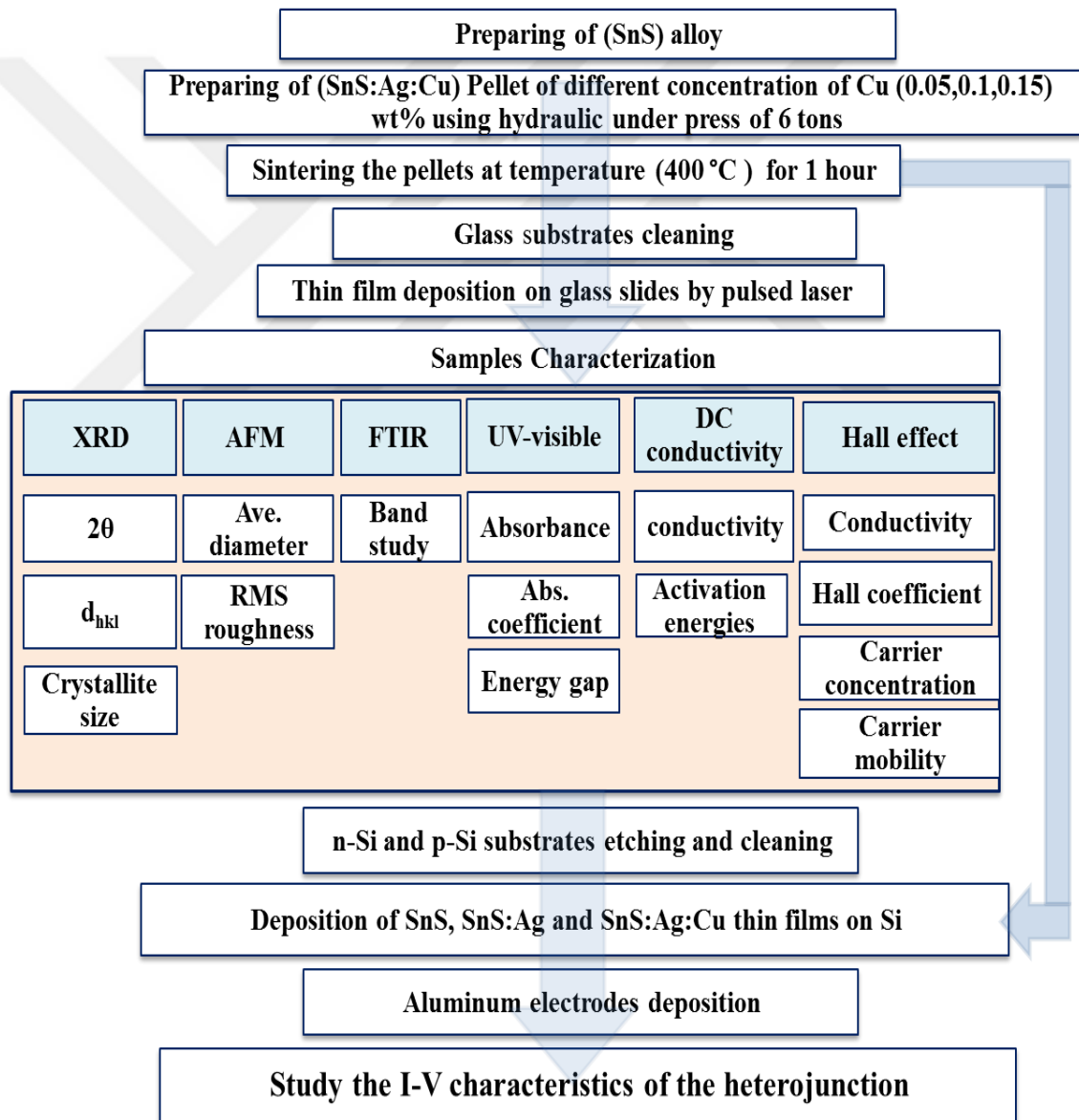


**Figure 3.1** Flow chart of experimental work

### 3.1 Preparation of Tin Sulfide

The  $\text{Sn}_x\text{S}_{1-x}$  were prepared by solid-state reaction route technique under vacuum. The same atomic ratio of (99.999%) purity (Sn and S) elements according to their atomic percentages (Sn: S=0.5:0.5) were weighed using a four-digit electronic balance. The mixed elements were sealed in an evacuated ( $\sim 10^{-3}$  Torr) quartz ampoule (length 20 to 25 cm and internal diameter  $\sim 8$  mm). The ampoules were heated to  $1200^\circ\text{C}$  for 5 hours, according to the phase diagram of the Sn-S system, then cooled to room temperature. The temperature of the furnace was increased at a rate of  $10^\circ\text{C}/\text{min}$ . Figure 3.2 shows the phase diagram and the used Furnace (CARBOLITE).

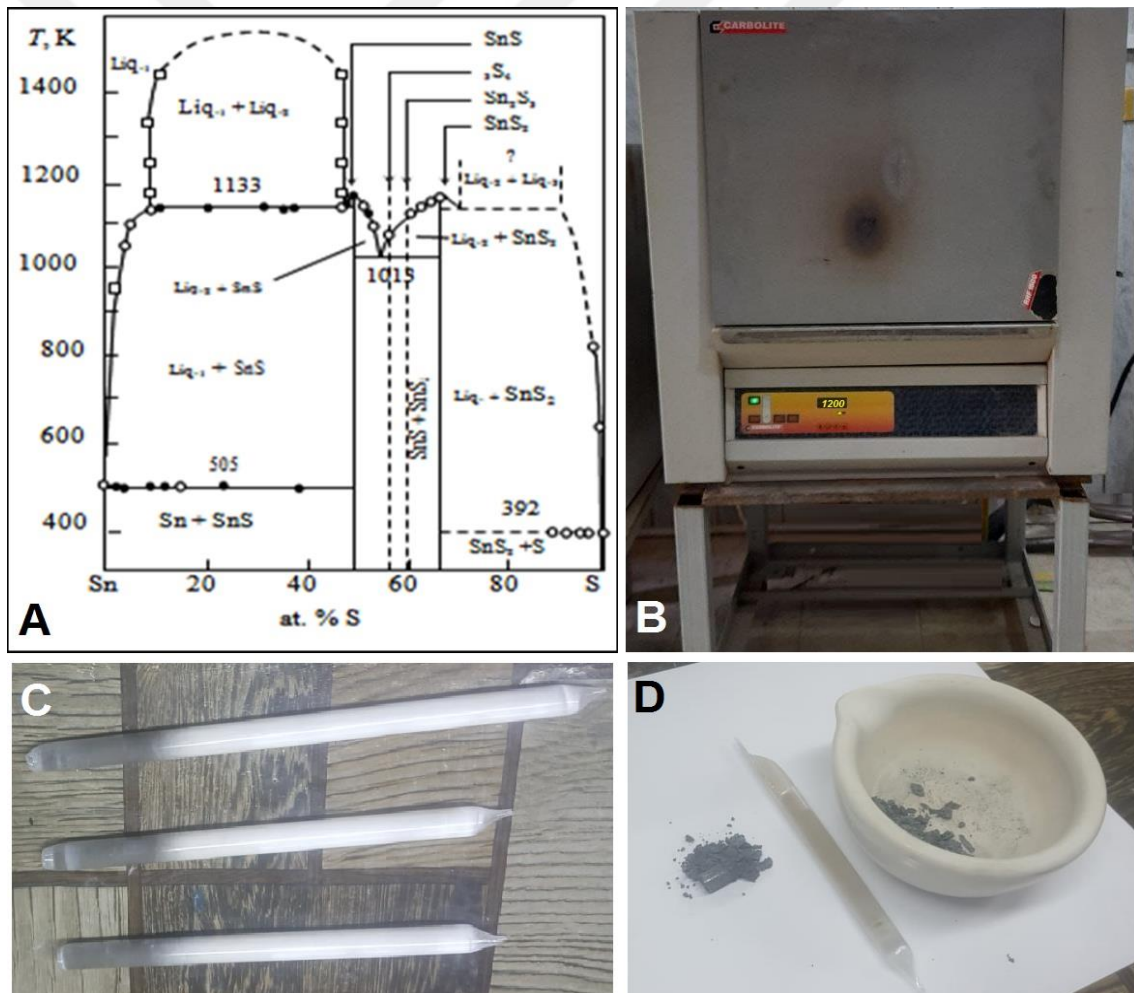


**Figure 3.2** (A) Phase diagram of Sn-S system, (B) the used furnace, (C) vacuumed ampoules containing Sn+S, and (D) opening ampoules after cooling.

### 3.2 Preparation of Pellets

The prepared SnS was mixed with silver Ag (of 9 at %) from Nanjing Nano Technology Co. Ltd with a purity of 99.99% and Copper Cu from Chem-Lab NV with the purity of 99.5% were mixed at different concentration of  $x = (0.05, 0.1, \text{ and } 0.15)$  wt. %. The powder of precursors was mixed using a gate mortar for one hour. It was pressed into pellets of 1cm diameter and 0.2 cm thickness, using a hydraulic press type (SPECAC), under press of 6 tons for 10 minutes. Figure 3.3 shows the steps of pellet preparation.

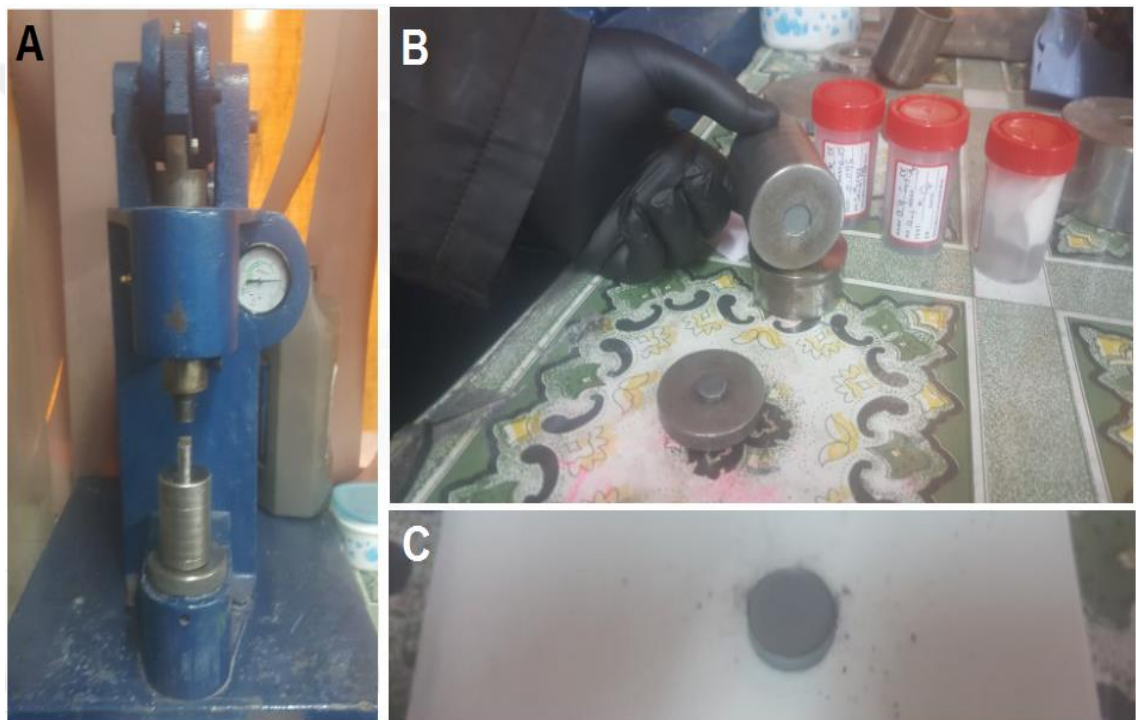


**Figure 3.3** Preparation pellet steps (A) pressing powder in a mold, (B) taking away the pellet, and (C) the final pellet

### 3.3 Preparation of Substrates

Considering they significantly affect the characteristics of the deposited films, the substrate's nature and purity is crucial factor.

### 3.3.1 Glass slides

In this study, we used glass as substrates for deposition, to study the structural, optical and electrical properties of (SnS, SnS: Ag, SnS: Ag: Cu) thin films, because its low cost and the results are not affected by the amorphous structure. Glass slides 1.25× 1 cm<sup>2</sup> area was used to deposit the thin films. The procedure of cleaning the glass slides could be explained briefly as follows:

- They were washed softly for 15 minutes under running water after being washed with soap and water to remove any oil or dust from the surface of the used slides.
- They were cleaned a 15-minutes ultrasonically followed by rinsing in distilled water (DW).
- Next, we repeat step 2 with pure alcohol instead of DW, which reacts with contaminants like oil and some oxide.
- Finally, soft paper is used to wipe the slides after they have been dried with air blowers.

### 3.3.2 Silicon substrate

An n-type and p-type Si slides were used (opposite type than the deposited material type) with crystal orientation (100) as a substrate for the construction of the photovoltaic devices of (SnS, SnS: Ag and doped SnS: Ag at different Cu ratios). The Si wafers were cleaned and etched using diluted hydrofluoric acid with distilled water at (1:10) for 10 mins. then washed with DW, as a final point dried by blowing air.

## 3.4 Deposition Equipment

The chamber and all the parts related to it, such as vacuum pumps (rotary pumps), Perini indicators, the target and substrate holders, are also important parts of the PLD system in addition to the laser source.

### 3.4.1 Nd: YAG laser source

The (SnS, SnS: Ag, and SnS: Ag: Cu) thin films were produced by the Nd: YAG laser (Huafei Tonged Technology—DIAMOND-288 pattern EPLS). The Neodymium doped yttrium aluminum garnet laser (Nd: YAG) is a solid-state system. Flash lamps in the exciting source. When the lasing process starts, the Q-switch enables the gain medium to attain the maximum population inversion. These are the primary technical criteria:

- Q-switched Nd: YAG laser is the kind of laser.
- Laser wavelength: 1064 nm.
- Pulse width: 10 ns.
- 6 Hz is the repetition rate.
- Inner circulation water-cooling is the cooling technique.

The light path system is in the form of the external handy piece. The power supply, controller, and cooling system are mounted inside the laser box. The laser is cooled using distilled water. The energy of each pulse can be increased by steps of 20 mJ. The size of the laser spot of 2 mm diameter, repetition frequency and number of pulses is controllable.

### 3.4.2 The procedure of thin film deposition by PLD

A vacuum glass of cylindrical shape has a 25 cm diameter and 30 cm height. Figure 3.4 shows the diagram of the experimental setup. The target is located on a horizontal holder inside the chamber. The substrate is fixed parallel to the surface of the target above it at 1.5 cm. The PLD procedure was carried out inside a vacuum of around ( $10^{-2}$  mbar). The concentrated 400 mJ 1064 nm Nd: YAG laser pulse, with pulse widths of 10 ns, repetition rates of 6 Hz, and 300 laser pulses, incident at a  $45^\circ$  angle on the target surface. Target and laser distances were calibrated to be equal to their respective focus lengths (10 cm). Figure 3.4 shows the pulsed laser deposition setup.

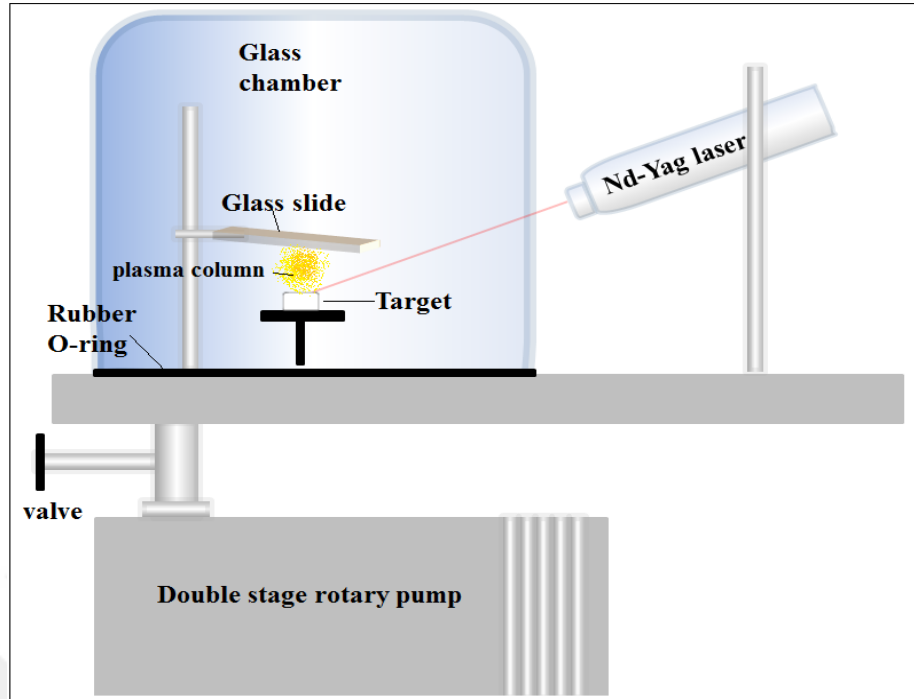


**Figure 3.4** Schematic of the experimental setup for the PLD technique

### 3.4.3 Thickness measurement

The thin film thicknesses were measured according to the principle of reflectance from thin films using an optical bench kit shown in Figure 3.5. He-Ne laser of 632 nm wavelength was used. The interference pattern is used to determine the film thickness ( $t$ ) according to the relation, Equation (3.1):

$$t = \frac{\lambda}{2} \frac{\Delta x}{x} \quad (3.1)$$

where  $\lambda$  is the used laser wavelength,  $x$  is the width of bright fringes,  $\Delta x$  is the thickness of dark fringes. The thin film thickness was  $250 \pm 10$  nm for all samples.

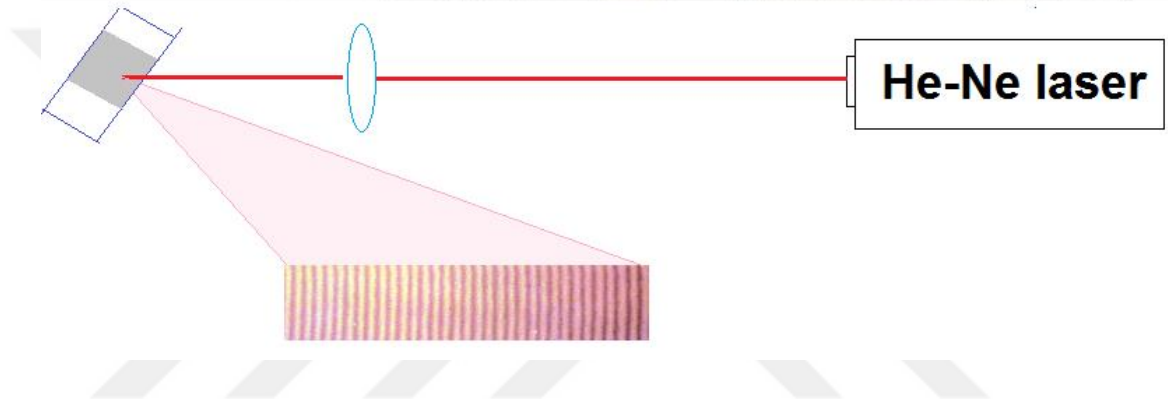
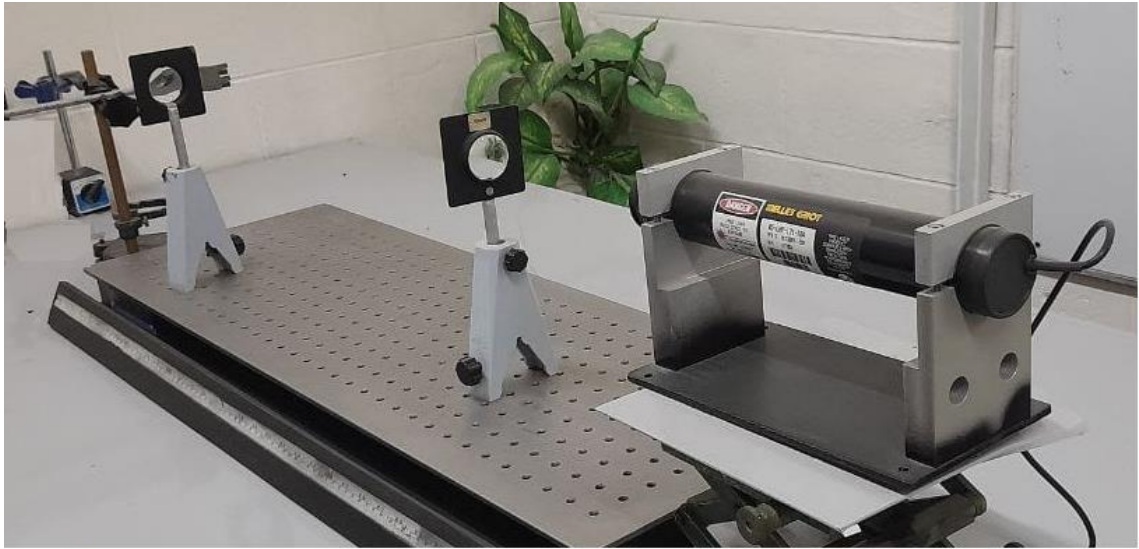


**Figure 3.5** Optical thickness measurement

### 3.5 Structural Properties

The crystal structure of (SnS, SnS: Ag, and SnS: Ag: Cu) thin films were examined by X-ray diffraction technique. When a beam of X-rays is fallen at a certain angle on the surface of a crystalline sample as a result of Bragg's reflections from the parallel crystal surfaces a diffraction pattern were formed. When the amorphous thin film was tested, the reflected pattern does not form any peaks, meaning that the interference of the reflected beams is destructive. But when the thin film is arranged in a crystalline feature, the interference is constructive, due to the reflection from regular crystals without any scattering by the beams reflected from those crystal surfaces as a result of their regularity. Thus, peaks appear indicating the constructive interference of the X-ray waves reflected from parallel crystal surfaces as a result of the fulfillment of Bragg's condition, Equation (3.2) (Bragg and Bragg 1915).

$$n \lambda = 2 d_{hkl} \sin \theta \quad (3.2)$$

Where  $n$  is the diffraction order,  $\lambda$  is the wavelength of the incident rays,  $d_{hkl}$  is the distance between two successive planes and  $\theta$  is the angle of incidence and reflection of an X-ray beam falling on a given surface. When knowing the angles corresponding to these peaks, the  $d_{hkl}$  value is determined through Bragg's law. And from  $d_{hkl}$  value Miller's coefficients ( $hkl$ ) are determined according to the standard card, and through those coefficients, the crystalline structure is determined.

X-ray diffraction device (LabX XRD-8000), shown in Figure 3.6, was used with the specifications:

- Source=Cu-K
- Current=30 mA
- Voltage=40KV
- Wave length=1.5406 Å
- Range of diffraction angle=20-80°
- Scanning speed=5 degree/min



**Figure 3.6** XRD system

The relation between the crystallite size ( $D$ ) and the full width at half maximum (FWHM) of diffraction lines was determined by the Debye-Scherrer formula, Equation (3.3) (Scherrer 1918):

$$D = \frac{0.9 \lambda}{FWHM \cdot \cos(\theta)} \quad (3.3)$$

While, the uniform strain of an induced lattice by defects or Nano-size effect, is determined according to the relation, Equation (3.4) (Raha and Das 2013):

$$\varepsilon = \frac{\beta \cos\theta}{4} \quad (3.4)$$

### **3.6 Surface Morphology**

Atomic Force Microscopy (AFM) is one of the most important devices used to diagnose of surface morphology in the nano range. It is used to identify the precise details of

topography about granular structures, their size distribution, and surface roughness. An AFM atomic force microscope (AA 3000 Scanning probe Microscope) supplied by Angstrom Advanced Inc. was used to study the surface topography of an (SnS, SnS: Ag, and SnS: Ag: Cu) film prepared on a glass substrate.

### 3.7 Optical Properties Measurements

The optical properties of the synthesized nanocomposite films deposited on glass substrates were examined. The UV-visible transmittance spectroscopy was used to study the optical properties of the thin films of SnS, SnS: Ag and SnS: Ag: Cu at different ratios of Cu (0.05, 0.10, and 0.15) deposited on glass slides. A two-beam UV/VIS Spectrophotometer (UV-1800 Shimadzu) as shown in Figure 3.7 was used at the spectral region (300-1100 nm). The sample on which the film is deposited is placed well in the base window so that the light rays fall perpendicular to the thin film. A glass slide similar to the used glass substrates is used as a reference to cancel out the effect of the glass and record only the film transparency. The collected data in the computer are used to calculate the optical absorbance, absorption coefficient, and energy band gap.



**Figure 3.7** UV-visible absorbance spectrometer

### 3.8 Electrodes Deposition

Three types of electrodes were used in our study as shown in Figure 3.8 for DC conductivity, Hall effect measurements, and mesh electrode for solar cell application. Aluminum electrodes were deposited by thermal evaporation using the Edward coating system at the high vacuum of 10<sup>-5</sup> mbar employing appropriate masks.

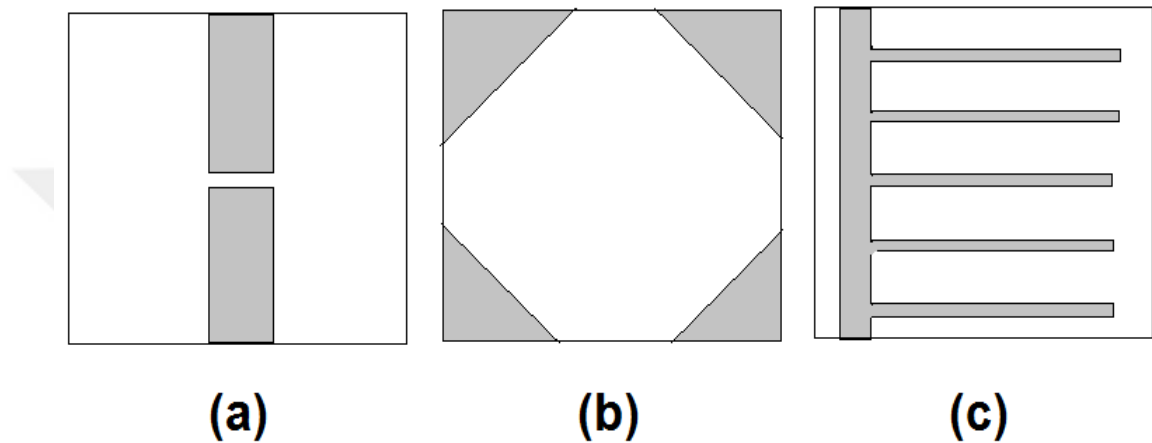


**Figure 3.8** Schemes of the three used electrodes for (a) DC conductivity, (b) Hall effect, and (c) solar cell application

### 3.9 Electrical Measurements

The measurement of semiconductor thin films' electrical characteristics enables the assessment of the materials' impurity levels and other crucial factors for their use in various electronic and optoelectronic applications. The electronic characteristics of a semiconductor are dependent on its nature, including whether it is pure, doped, or amorphous.

#### 3.9.1 D.C. conductivity measurement

The DC conductivity of the prepared thin films was examined using a multimeter connected with the samples placed over a controlled temperature hot plate to measure its resistance at different temperature. The sample conductivity then determine using the

electrode dimension. The relation between the sample conductivity and temperature is Equation (3.5):

$$\sigma = \sigma_0 \exp(-E_a/KT) \quad (3.5)$$

where  $\sigma$  is the semiconductor conductivity,  $\sigma_0$  the conductivity at high temperature,  $E_a$  activation energy,  $K$  boltzmann constant and  $T$  the absolute temprature.

### 3.9.2 Hall measurements

Hall effect measurements have been done by Hall measurement systems (Ecopia HMS-3000) as shown in Figure 3.9.



**Figure 3.9** Photograph for Hall measurement systems (Ecopia HMS-3000)

Measurements required four Ohmic contacts on the sample; has been added four-point probes into this device shown as in Figure 3.10 (a). The principle Hall effect refers to the potential difference (Hall voltage) in the lateral direction of a thin film semiconductor material through which an electric current is flowing, induced by a magnetic field ( $B=0.550$  Tesla) applied perpendicular to the sample as shown in the electric circuit (Figure 3.10) (b). The Hall coefficient ( $R_H$ ) was calculated using the change of the applied current with the generated inductive voltages according to Equation (2.10). The

kind of charge carrier depends on the Hall coefficient's sign. Equation (2.11) describes how the Hall coefficient and the carrier concentration ( $n_H$ ) are connected. Calculating the Hall mobility ( $\mu_H$ ) using Equation (2.12) was easy.

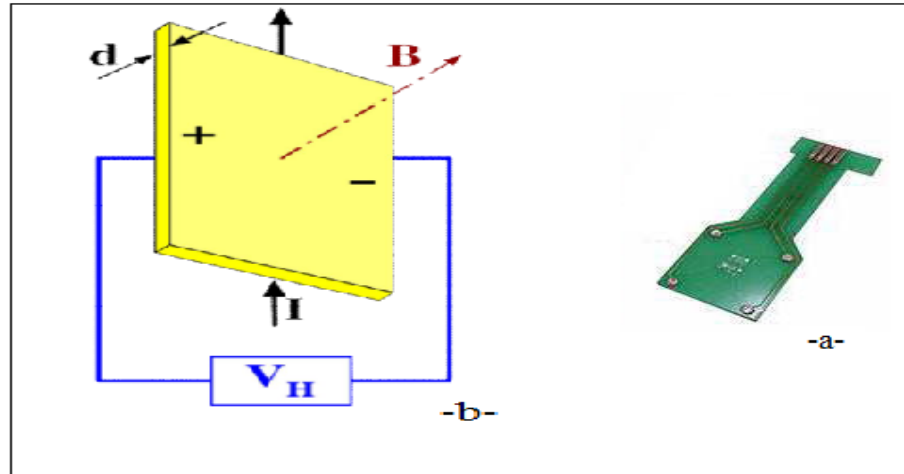


**Figure 3.10 (a) Sample board and (b) The electric diagram for Hall measurement**

### 3.10 Heterojunction Fabrication

After the etching and cleaning process of the silicon wafer, as explained previously, thin films of SnS, SnS: Ag, and SnS: Ag: Cu films were deposited using PLD technique on opposite types of Si wafers. Aluminum electrodes are completely covered the rear surface of a silicon wafer, and a mesh shape on the front surface. Thin and insulated wires are connected with aluminum electrodes using silver paste as shown in Figure 3.11.

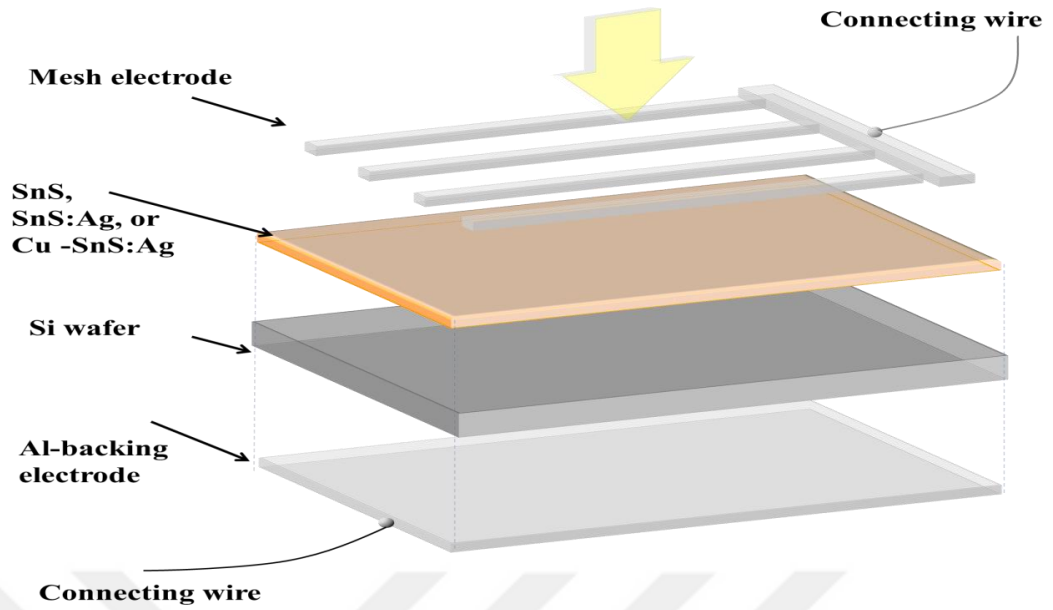


**Figure 3.11** Schematic diagram for heterojunction assembly

### 3.11 Current-Voltage Characteristics for Heterojunction

The I-V characteristics for the synthesized photovoltaic device based on SnS, SnS: Ag and Cu-doped SnS: Ag on Si heterojunction at dark and under illumination by halogen lamp, by using two digital multimeters and a D.C. power supply. The bias voltage was varied over the range of -2 to 2 Volt. The voltage was adjusted by fine-tuning the power supply. Figure 3.12 shows a schematic diagram for of the circuit used for I-V characteristics measurements.

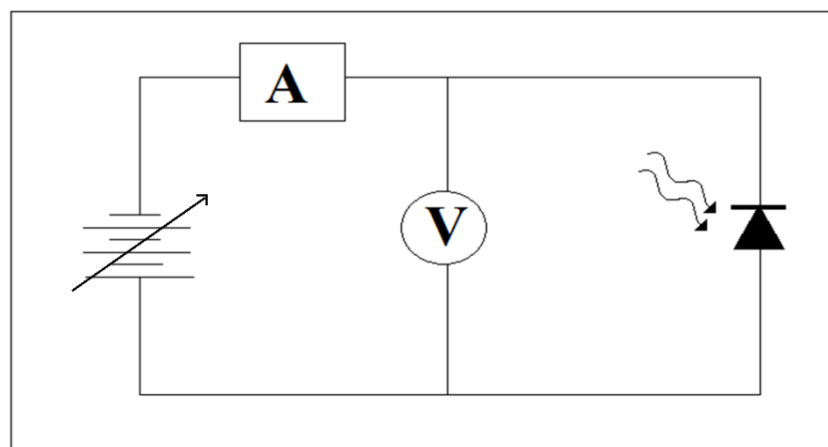


**Figure 3.12** Schematic diagram for the circuit of I-V characteristics measurements

## 4. RESULTS AND DISCUSSION

This section includes the results and discussion of the characterization of the SnS, SnS: Ag, Cu-doped SnS: Ag composites thin film at different Cu contents prepared by the pulsed laser deposition technique. The characterization includes X-ray diffraction, atomic force microscopy, UV-visible absorption, and Hall effect measurements. Finally, the results of solar cells based on SnS/Si, SnS: Ag/Si and SnS: Ag-Cu/Si heterojunctions were presented and discussed.

### 4.1 X-ray Diffraction Results

Figure 4.1 shows the X-ray diffraction (XRD) pattern for the used SnS powder, prepared by solid-state reaction route under vacuum, compared with the standard diffraction lines card no. (96-810-4282). The polycrystalline structure of pure orthorhombic SnS phase identical to the standard lines has appeared.

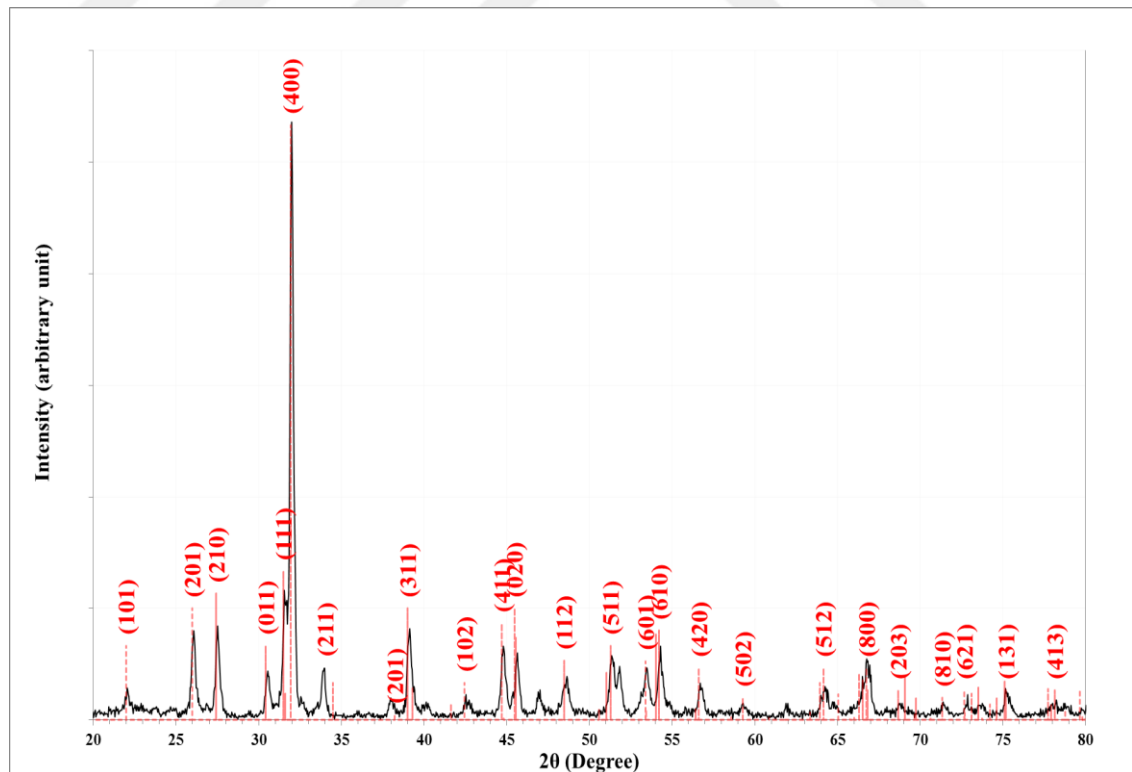


**Figure 4.1** X-ray diffraction pattern for SnS powder

The inter molecular plans spacing ( $d_{hkl}$ ) were determined using Bragg's formula in Equation (3.2), while the crystallite size ( $D$ ) in Equation (3.3) was determined according to Debye-Scherrer's formula using the full width at half maxima for the diffraction lines. Table 4.1 illustrates the XRD parameters for the diffraction peaks. The average crystalline size was 23.8 nm.

**Table 4.1** X-ray diffraction parameters ( $2\theta$ , FWHM,  $d_{hkl}$ ,  $D$ ,  $hkl$ ) for the SnS pellet

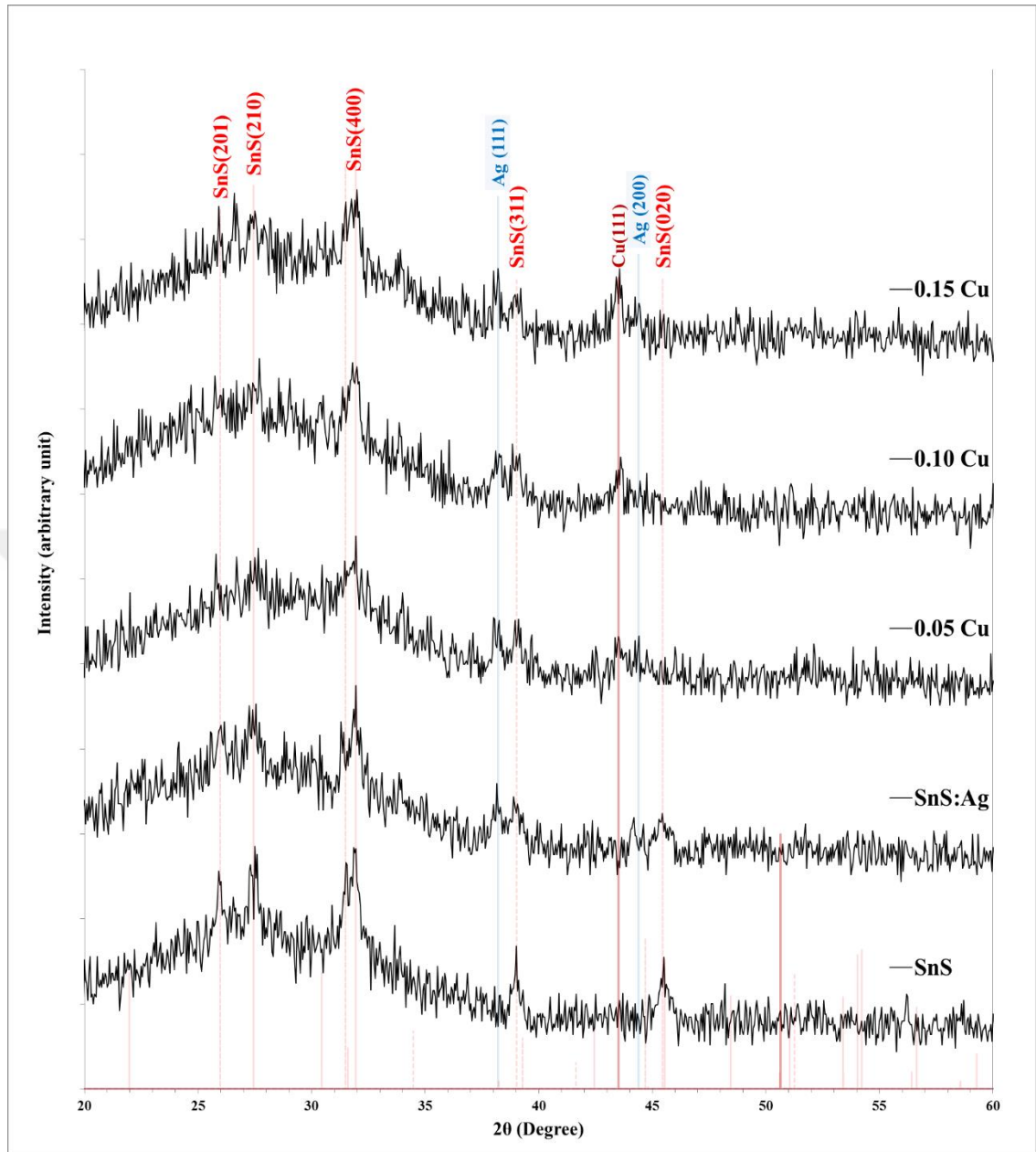
$2\theta$ (Deg.)	FWHM (Deg.)	$d_{hkl}$ Exp.(Å)	$D$ (nm)	$hkl$
22.0357	0.3000	4.0306	27.0	(101)
26.0857	0.3215	3.4132	25.4	(201)
27.5000	0.3429	3.2408	23.9	(210)
30.5857	0.3429	2.9205	24.0	(011)
31.5714	0.3214	2.8316	25.7	(111)
32.0000	0.2786	2.7946	29.7	(400)
33.9500	0.3214	2.6384	25.8	(211)
37.9786	0.3857	2.3673	21.8	(201)
39.1357	0.3643	2.2999	23.1	(311)
42.6071	0.4929	2.1202	17.3	(102)
44.8143	0.3643	2.0208	23.6	(411)
45.6286	0.3858	1.9866	22.3	(200)
48.5643	0.4929	1.8732	17.7	(112)
51.3929	0.4072	1.7765	21.7	(511)
53.4071	0.3214	1.7142	27.7	(601)
54.2857	0.3643	1.6885	24.5	(610)
56.7071	0.3643	1.6220	24.8	(420)
59.3429	0.3857	1.5561	23.7	(502)
64.2286	0.4500	1.4490	20.8	(512)
66.7571	0.5786	1.4001	16.4	(800)
68.7500	0.3429	1.3643	28.1	(203)
71.4286	0.3643	1.3196	26.9	(810)
72.8000	0.3858	1.2981	25.6	(621)
75.2000	0.4286	1.2625	23.4	(131)

Figure 4.2 shows the XRD patterns for the prepared thin films by PLD technique of SnS, and SnS: Ag at different Cu ratios compared with the standard diffraction lines of the standard card no. 96-810-4282 Polycrystalline structure with low crystallinity appeared for all samples. All peaks appeared as broad features indicate on a nanocrystalline structure. For the SnS thin films the diffraction lines located at diffraction angles ( $2\theta$ )  $25.9113^\circ$ ,  $27.5158^\circ$ ,  $31.8790^\circ$ ,  $39.0007^\circ$ , and  $45.4750^\circ$  corresponding to the crystalline planes (201), (210), (400), (311), and (020) for the orthorhombic SnS structure. These

diffraction lines were slightly shifted after composing with silver due to strain in the lattice as a result of the incorporation of strange ions within the host lattice, or due to variation in crystallite size. Additional diffraction lines at  $2\theta = 38.1844^\circ$ , and  $44.2083^\circ$  appeared corresponding to crystal planes of (111), and (200) for cubic Ag, respectively, according to the standard card (96-901-2432).

Small variation in the diffraction pattern after doping with 0.05 Cu, while an additional peak for the diffraction plane (111) corresponding to the copper structure is located at  $43.5327^\circ$  according to standard card no. (96-500-0217) appeared for samples doped with a higher ratio. The appearance of the new phase at high doping concentration indicates that the added ratio exceeds the solubility limit of the host matrix. The addition of a small number of dopant impurities leads to a solid solution of the dopants. Increasing the doping concentration beyond the low solubility limit leads to supersaturated solutions in the host lattice, so appeared as a separate phase (Higler and Sprakel 2017).

The line breadth varies according to the Cu ratio indicating that this ratio affects the growth of nanoparticles due to the difference in nanoparticles growth. The  $d_{hkl}$  values were determined using the Bragg's formula, while the crystallite size ( $D$ ) was determined according to Debye-Scherrer's formula. The lattice strain induced after the doping process was determined using Equation (3.4). Table 4.2 illustrate the XRD parameters for the diffraction peaks. The result patterns agree with the previous study (Sebastian *et al.* 2022).



**Figure 4.2** X-ray diffraction patterns of the thin films prepared by PLD technique for SnS, SnS: Ag, and Cu-doped SnS: Ag at different ratios

**Table 4.2** X-ray diffraction parameters for the thin films prepared by PLD for SnS, SnS: Ag, and Cu-doped SnS: Ag at different ratios

Sample	2θ (Deg.)	FWHM (Deg.)	$d_{hkl}$ Exp.(Å)	D (nm)	hkl	Phase	Lattice strain
SnS	25.9113	0.3096	3.4358	26.3	(201)	Orth. SnS	0.0013
	27.5158	0.4504	3.2390	18.2	(210)	Orth. SnS	0.0019
	31.8790	0.4504	2.8049	18.3	(400)	Orth. SnS	0.0019
	39.0007	0.5348	2.3076	15.8	(311)	Orth. SnS	0.0022
	45.4750	0.5348	1.9930	16.1	(020)	Orth. SnS	0.0022

**Table 4.2** X-ray diffraction parameters for the thin films prepared by PLD for SnS, SnS: Ag, and Cu-doped SnS: Ag at different ratios (Continued)

Sample	2 $\theta$ (Deg.)	FWHM (Deg.)	$d_{hkl}$ Exp.(Å)	D (nm)	hkl	Phase	Lattice strain
SnS: Ag	25.9958	0.4786	3.4248	17.0	(201)	Orth. SnS	0.0020
	27.4032	0.6475	3.2521	12.6	(210)	Orth. SnS	0.0027
	31.9071	0.5348	2.8025	15.4	(400)	Orth. SnS	0.0022
	38.1844	0.5630	2.3550	14.9	(111)	Cub. Ag	0.0023
	38.9726	0.5348	2.3092	15.8	(311)	Orth. SnS	0.0022
	44.2083	0.4504	2.0471	19.0	(200)	Cub. Ag	0.0018
	45.4469	0.8163	1.9941	10.6	(020)	Orth. SnS	0.0033
0.05 Cu	27.6284	0.6756	3.2261	12.1	(210)	Orth. SnS	0.0029
	31.8508	0.6474	2.8074	12.8	(400)	Orth. SnS	0.0027
	38.1562	0.4786	2.3567	17.6	(111)	Cub. Ag	0.0020
	39.0852	0.3940	2.3028	21.4	(311)	Orth. SnS	0.0016
	43.5327	0.4786	2.0773	17.9	(111)	Cub. Cu	0.0019
0.10 Cu	27.4314	0.6474	3.2488	12.6	(210)	Orth. SnS	0.0027
	31.9071	0.5912	2.8025	14.0	(400)	Orth. SnS	0.0025
	38.2970	0.6193	2.3483	13.6	(111)	Cub. Ag	0.0026
	39.0007	0.5066	2.3076	16.6	(311)	Orth. SnS	0.0021
	43.5890	0.5067	2.0747	16.9	(111)	Cub. Cu	0.0021
0.15 Cu	25.9395	0.6474	3.4321	12.6	(201)	Orth. SnS	0.0028
	27.4877	0.5067	3.2423	16.1	(210)	Orth. SnS	0.0021
	31.8790	0.5630	2.8049	14.7	(400)	Orth. SnS	0.0024
	38.1562	0.5067	2.3567	16.6	(111)	Cub. Ag	0.0021
	39.0570	0.5348	2.3044	15.8	(311)	Orth. SnS	0.0022
	43.5327	0.5349	2.0773	16.0	(111)	Cub. Cu	0.0022
	44.3772	0.5911	2.0397	14.5	(200)	Cub. Ag	0.0024

Figure 4.3 shows the variation of crystallite size and lattice strain along the (400) direction (which is the preferred orientation) of the SnS: Ag and Cu-doped SnS: Ag thin films prepared by the PLD technique with the Cu ratio. It seems that the crystallite size reduced from 15.4 to 12.8 nm after doping with 0.05 Cu, then it increased to 14 and to 14.7 with an increasing Cu ratio to 0.10 and 0.15, respectively, while the lattice strain has opposite behavior indicating that the main cause of lattice contraction due to nano-size effect as a result of the surface tension by the surface atoms in nanoparticles. This effect is very large at small sizes due to the increase in the area-to-volume ratio (Huang *et al.* 2007).

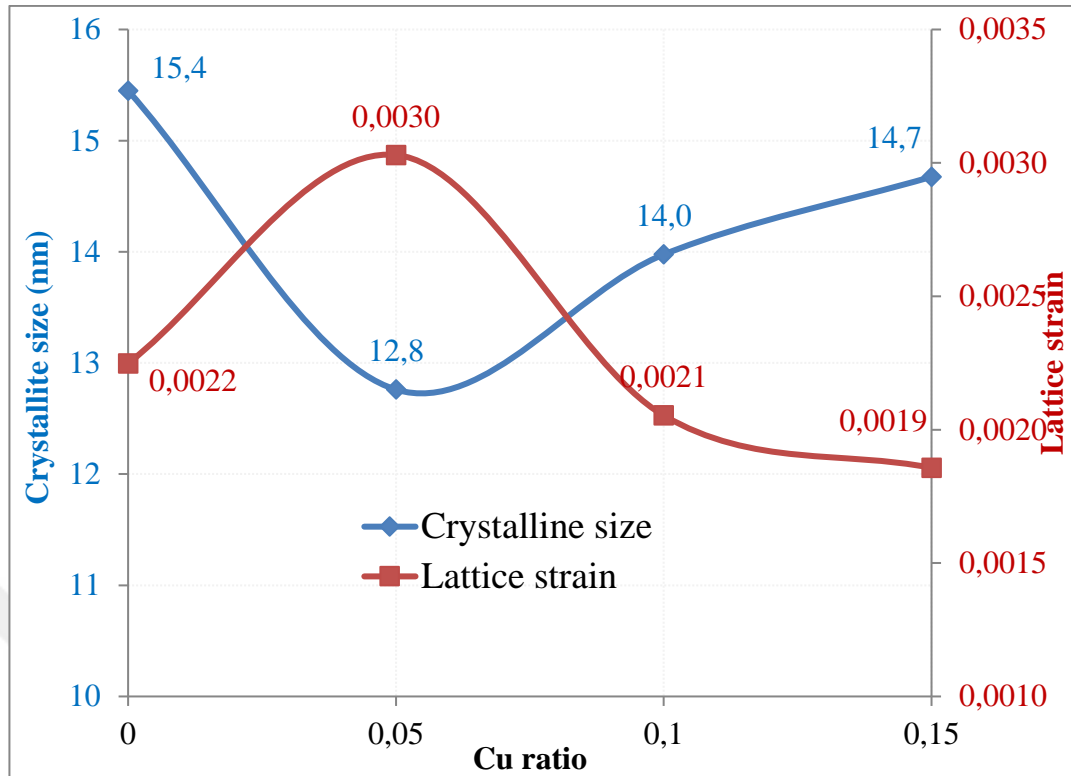


**Figure 4.3** Variation of crystalline size and lattice strain of the thin films prepared by PLD technique for Cu-doped SnS: Ag with the Cu ratio

## 4.2 Atomic Force Microscopy

Figure 4.4 displays the atomic force microscopy images for the SnS, SnS: Ag, and Cu-doped SnS: Ag thin films at different Cu ratios, and their particle size distribution histogram. The surface of the SnS thin film appeared of a high degree of roughness and large particle size.

The particle distribution histogram attached to the figures shows a wide particle size distribution with multiple modes. For SnS: Ag-doped with 0.05 Cu is with lower roughness, and the smallest particle diameter is at 0.10 Cu. Increasing the Cu percentage to 0.15 caused to increase in the surface roughness and average particle size. The particle size distribution appeared at the highest Cu content in a single pattern with an average particle diameter of 81.60 nm (Table 4.3).

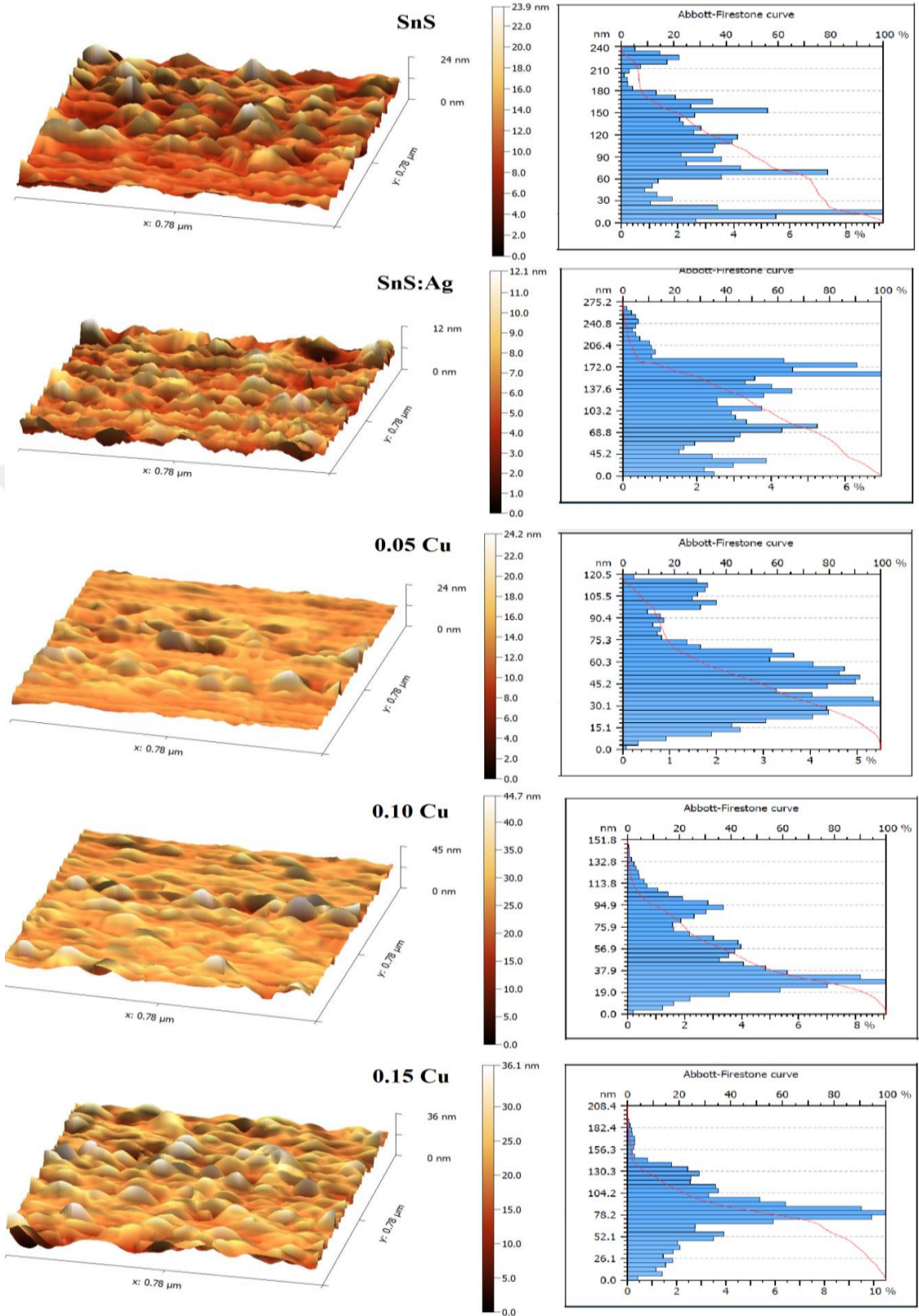


**Figure 4.4** AFM images for the thin films of SnS, SnS: Ag and Cu-doped SnS: Ag at different Cu ratios

**Table 4.3** AFM parameters for the thin films prepared PLD for Cu-doped SnS: Ag at different Cu ratios.

Sample	Average Diameter (nm)	RMS roughness (nm)
SnS	115.5	2.72
SnS: Ag	110.3	2.20
0.05 Cu	48.70	1.16
0.10 Cu	37.50	1.54
0.15 Cu	81.60	2.78

### 4.3 Furrier Transform Infrared Spectroscopy Results

To learn more about the potential structural components of the deposited thin films, FT-IR spectroscopy has been used. Figure 4.5 shows the Furrier transform infrared spectroscopy (FTIR) patterns for the SnS, SnS: Ag, and Cu-doped SnS: Ag thin films deposited at different Cu ratios. Several well-defined absorption bands were observed in the spectra at about 3394.83, 2925.00, 2854.17, 2362.50, 2327.17, 1612.43, 1437.50, 1045.83, and 633.33  $\text{cm}^{-1}$

A broad band at 3394.83  $\text{cm}^{-1}$  indicates stretching vibrations of O–H. The two bands at 2925.00 and 2854.17  $\text{cm}^{-1}$  are assigned to the asymmetric and symmetric vibrations of  $\text{CH}_2$  (Aksay *et al.* 2009). The double band located at 2362.50 and 2327.17  $\text{cm}^{-1}$  is assigned to O=C=O vibrations in carbon dioxide (Toda *et al.* 2013). The band at 1045.83 $\text{cm}^{-1}$  comes from the vibration of C–S (Aksay *et al.* 2009). The absorption bands located at 1437.50 and 633.33  $\text{cm}^{-1}$  indicates the Sn-S bands (Kihal *et al.* 2017). Moreover, the appearance of the band at 1612.43  $\text{cm}^{-1}$  corresponds to the C-O band (Umar *et al.* 2013). The bands corresponding to strange atoms in the film probably come from the ambient.

As shown in Table 4.4, most bands shifted towards a higher wavenumber after doping with Ag, as well as an increase in the percentage of Cu doping indicates that Ag and Cu ions are successfully incorporated into the SnS matrix (Srivind *et al.* 2018).

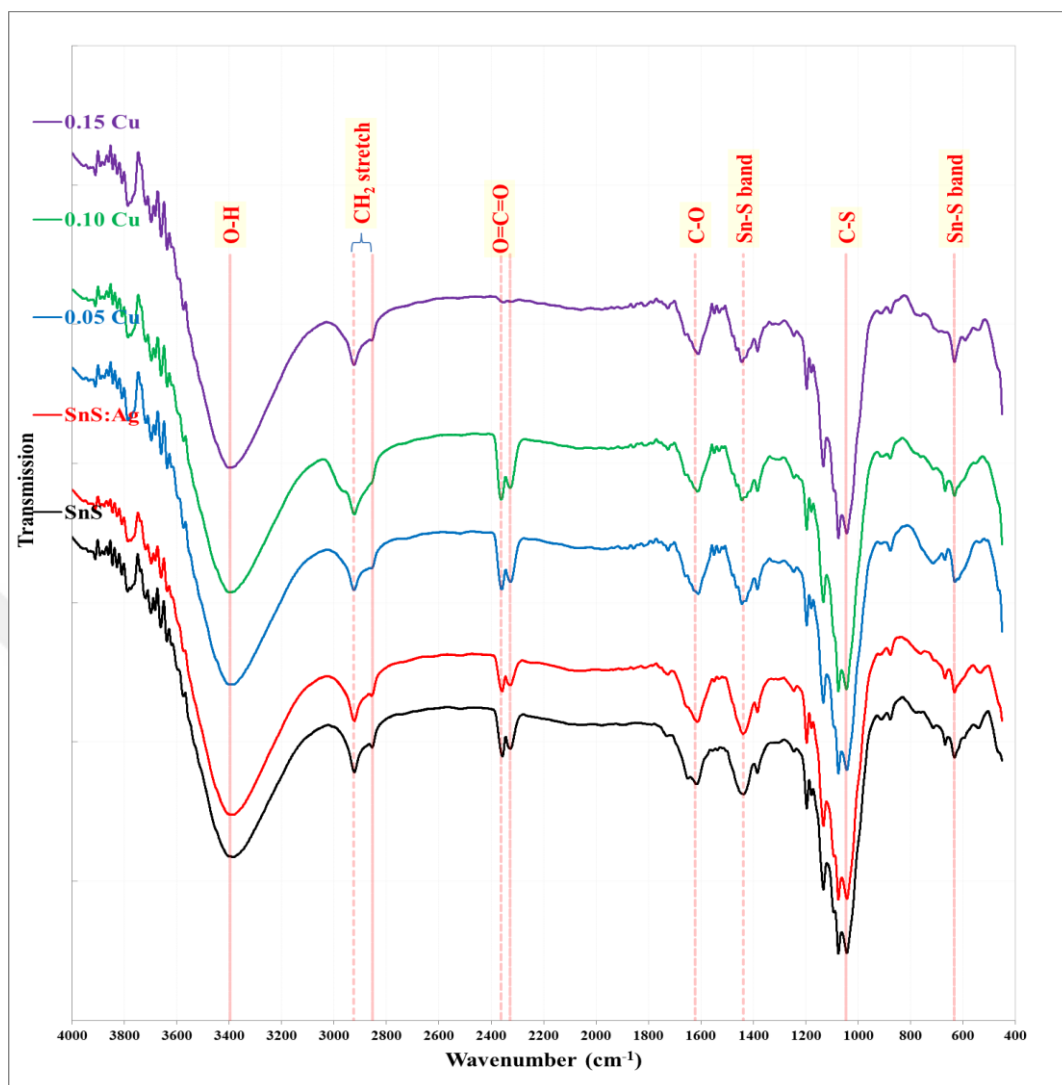


**Figure 4.5** FTIR patterns for the SnS, SnS: Ag and doped SnS: Ag at different Cu ratios

**Table 4.4** FTIR bands for the thin films of SnS: Ag and Cu-doped SnS: Ag at different Cu ratios

Band Type	SnS	SnS: Ag	0.05 Cu	0.10 Cu	0.15 Cu
O-H stretch	3394.83	3395.22	3395.93	3404.17	3400.20
CH <sub>2</sub> Stretch	2925.00	2920.83	2923.66	2924.90	2925.00
	2854.17	2862.50	2870.83	-	-
O=C=O	2362.50	2363.40	2363.65	2363.77	-
	2327.17	2327.17	2328.22	2329.00	-
C-O	1612.43	1614.50	1615.60	1617.31	1618.20
Sn-S	1437.50	1437.50	1441.67	1441.77	1445.83
C-S	1045.83	1041.67	1037.50	1041.67	1045.83
Sn-S	633.33	629.17	625.00	633.33	629.17

## 4.4 Optical Properties

### 4.4.1 UV-visible absorbance

Figure 4.6 shows the absorbance curves for the deposited SnS, SnS: Ag, and Cu-doped SnS: Ag thin film samples at different Cu ratios. It appeared that the absorbance gradually decreased with wavelength indicated on low crystallinity for all samples, as shown by the XRD. Strong absorption at short wavelengths and low absorption at long wavelengths; only photons with enough energy can interact with semiconductors to produce electron-hole pairs (Jose *et al.* 2017). It was observed that the absorbance increases for the SnS: Ag sample compared with the SnS sample, in addition, increasing the Cu content causes more increase in absorption due to creating localized levels within the energy bandgap, which acts as a springboard to promote the electronic transition. The red shift is the most obvious with Cu doping and significantly improves absorption in the visible range compared with other transition metals (Gao *et al.* 2021).

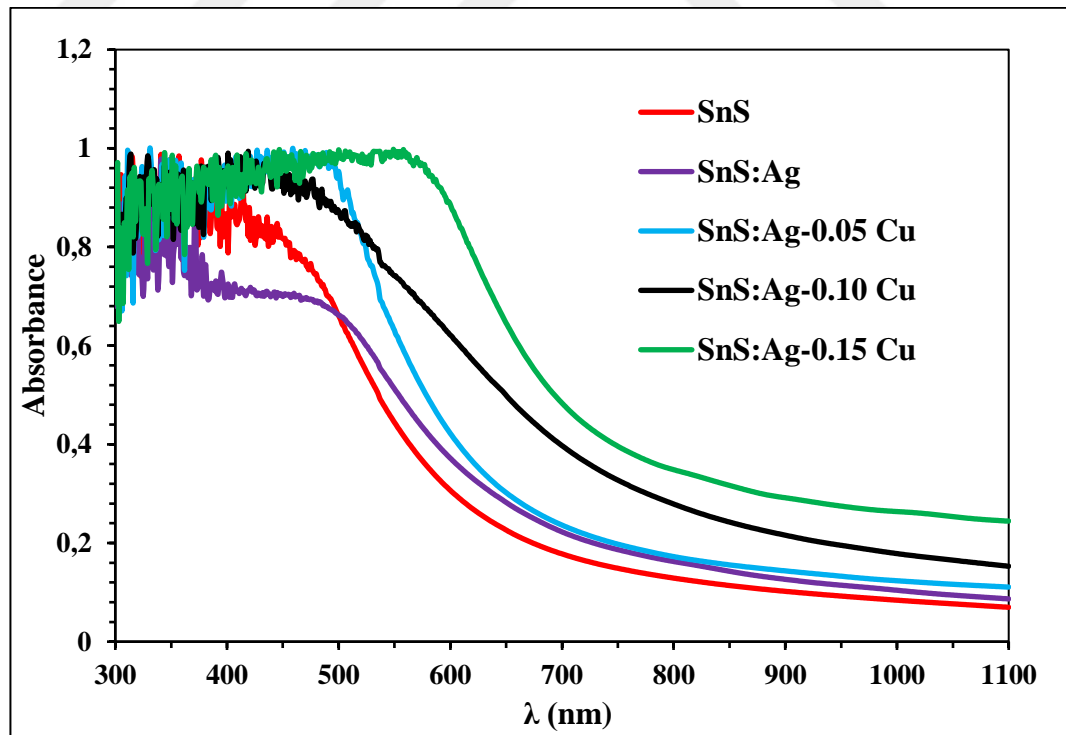


**Figure 4.6** UV-visible absorbance spectra for the thin films of SnS, SnS: Ag, and Cu-doped SnS: Ag at different Cu ratios

#### 4.4.2 Absorption coefficient

The absorption coefficient ( $\alpha$ ) for SnS, SnS: Ag, and Cu-doped SnS:Ag thin film samples at different Cu ratios were determined according to Equation (2.7). The variation of  $\alpha$  with wavelength was shown in Figure 4.7. It has the same behavior as absorption spectra. The absorption coefficient in the range of  $10^4$ , especially at low wavelengths indicate the direct electronic transition (Baco *et al.* 2012).

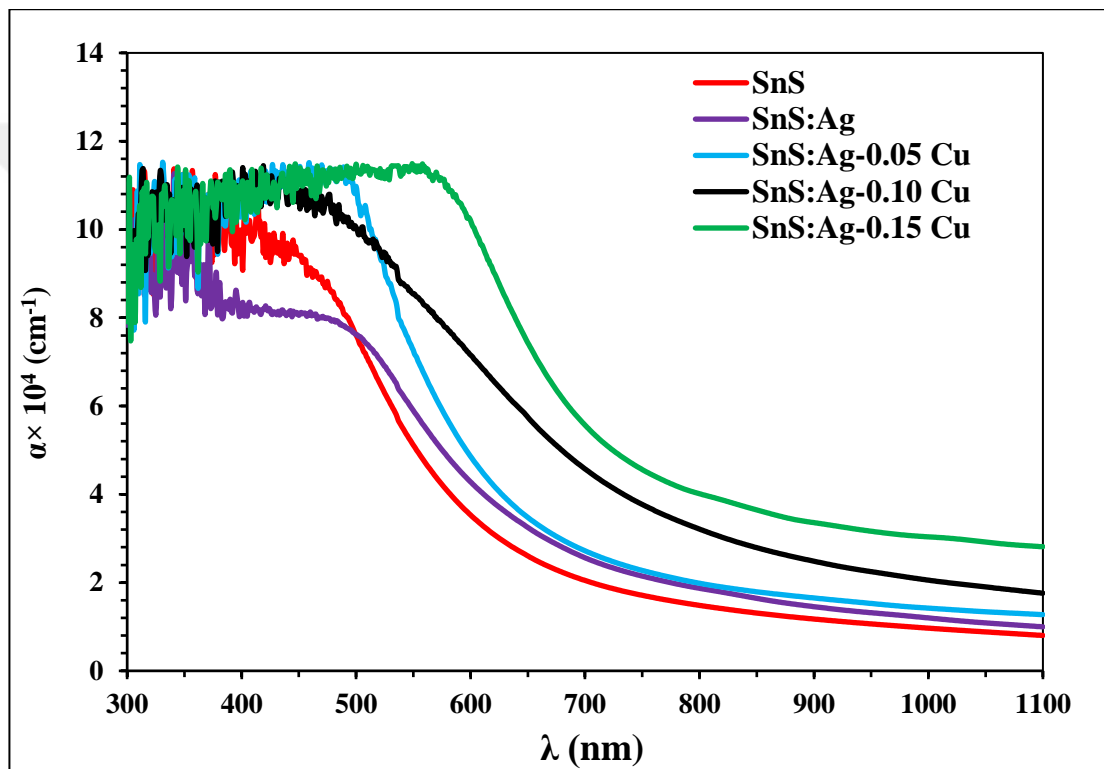


**Figure 4.7** Absorption coefficient for the thin films prepared by PLD for Cu-doped SnS: Ag at different Cu ratios

#### 4.4.3 Optical energy gap

The optical energy bandgap ( $E_g^{opt}$ ) for the SnS, SnS: Ag, and Cu-doped SnS: Ag thin films at different Cu ratios deposited by pulsed laser on glass slides were determined by using the Tauc formula as shown in Figure 4.8. This formula is used to determine the type of electronic transition by plotting the relations  $(\alpha h\nu)^{1/2}$ ,  $(\alpha h\nu)^{1/3}$ ,  $(\alpha h\nu)^{2/3}$ , and  $(\alpha h\nu)^2$  against  $h\nu$  to find the best linear behavior. For all samples, the best linear relation was for

$(\alpha h\nu)^2$  which conformed to the allowed direct electronic transition behavior. The optical bandgap equals the cross point of the tangential line with the x-axis. The bandgap reduced from 2.2eV to 2.05 eV when the SnS sample compose with Ag. Doping the SnS: Ag sample with Cu cause more reduction of energy bandgap to 2.0, 1.8, and 1.75 eV at 0.05, 0.10, and 0.15 Cu ratios, respectively. The band gap values are close to the reported values (Sebastian *et al.* 2022). The increase in direct band gap compared to the bulk SnS (1-1.3 eV) are due to the quantum confinement effect (Dar *et al.* 2021). Decreasing the band gap with increasing the metallic ions contents due to the creation of localized states near the valance and conductive bands (Norton *et al.* 2019). Table 4.5 shows the optical energy band gap for the SnS, SnS: Ag, and Cu-doped SnS: Ag thin films prepared at different Cu ratios by PLD.

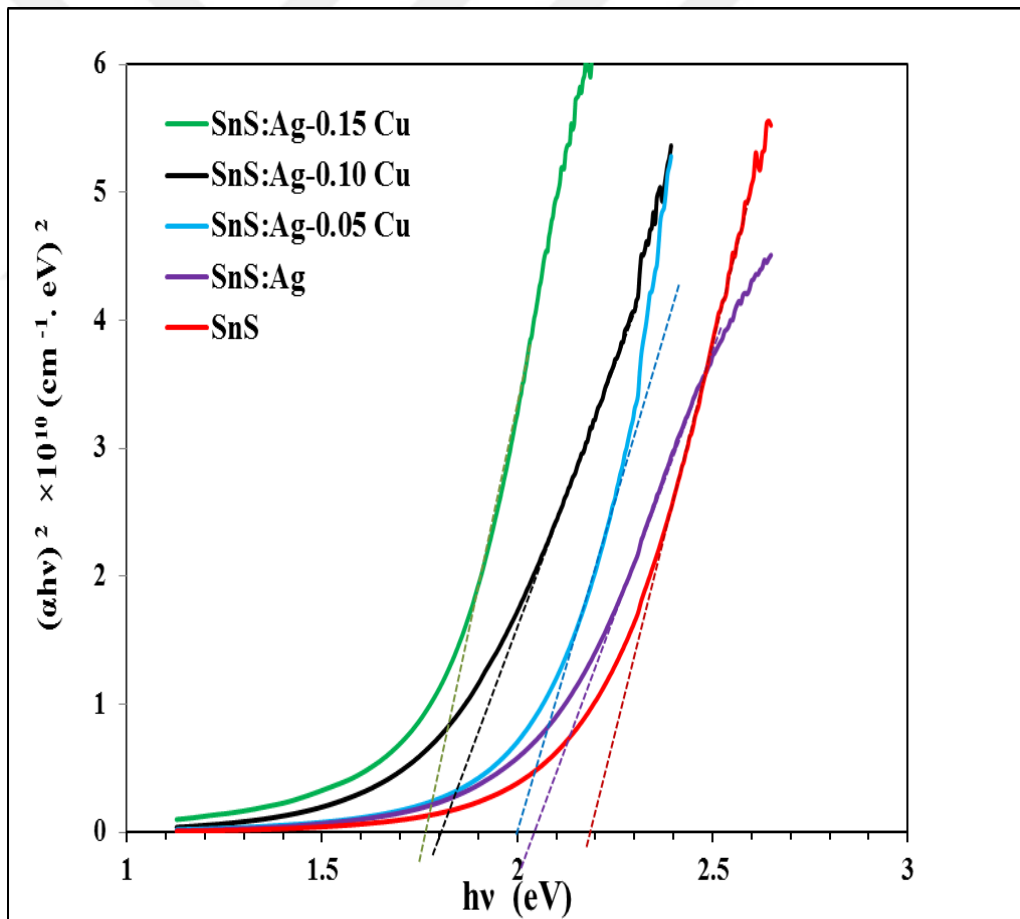


**Figure 4.8** Calculation of energy gap for the SnS, SnS: Ag, and Cu-doped SnS: Ag thin films prepared at different Cu ratios by PLD

**Table 4.5** Optical energy band gap  $E_g^{Opt}$  for the SnS, SnS: Ag, and Cu-doped SnS: Ag thin films prepared at different Cu ratios by PLD.

Sample	$E_g$ (eV)
SnS	2.20
SnS:Ag	2.05
0.05 Cu	2.00
0.10 Cu	1.80
0.15 Cu	1.75

#### 4.5 Direct Current Conductivity Results

The direct current conductivity for the SnS, SnS: Ag, and Cu-doped SnS: Ag thin films at different Cu ratios deposited by pulsed laser on glass slides were investigated as shown in Figure 4.9. According to Equation (2.8), from the relation between the logarithm of sample conductivity with the reverse of temperature, the activation energies can be calculated from the slope of the best linear fit. The figure shows two activation energies (two linear behaviors at two temperature regions) for each sample. The activation energies and their ranges were illustrated in Table 4.5. As shown in Figure 4.10, the activation energy values are less than half of the energy band gap. Both activation energies are reduced by adding Ag and by increasing the Cu content as a result of shifting the Fermi level with the doping ratio (Tietze *et al.* 2012). This shifting caused to enhancement of the sample conductivity as shown in Table 4.6.

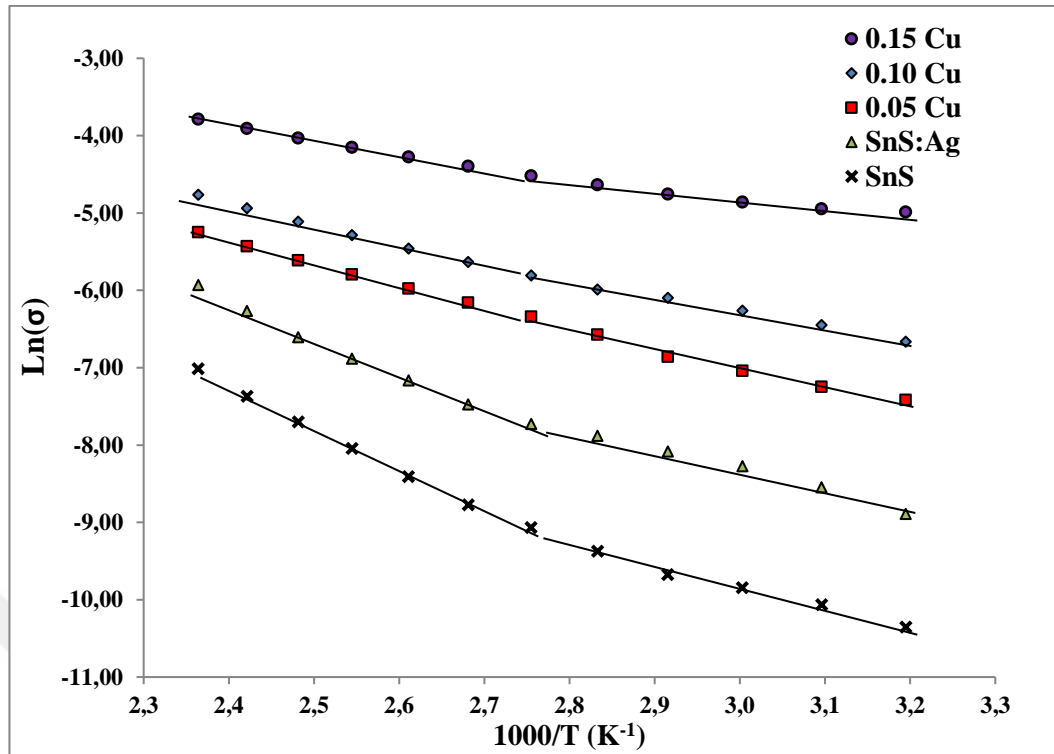


**Figure 4.9** Logarithm of DC conductivity versus the temperature inverse for SnS, and Cu-doped SnS: Ag thin films at different Cu ratios

**Table 4.6** Activation energies and their ranges for the SnS, and Cu-doped SnS: Ag at different Cu ratios thin films

Sample	$E_{a1}$ (eV)	Range (K)	$E_{a2}$ (eV)	Range (K)	$\sigma_{RT}$ ( $\Omega^{-1} \cdot \text{cm}^{-1}$ )
SnS	0.242	313-363	0.457	363-423	3.19E-05
SnS:Ag	0.226	313-363	0.395	363-423	1.38E-04
0.05 Cu	0.212	313-363	0.241	363-423	6.00E-04
0.05 Cu	0.163	313-363	0.230	363-423	1.28E-03
0.05 Cu	0.094	313-363	0.162	363-423	6.80E-03

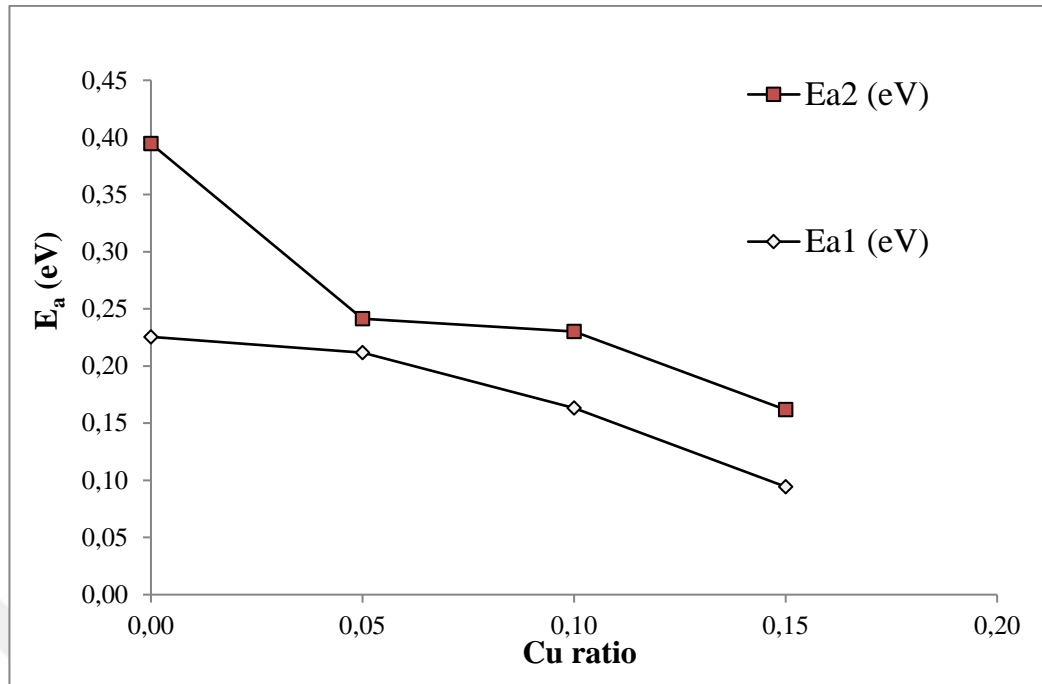


**Figure 4.10** Variation of the two activation energies with Cu ratio for Cu-doped SnS: Ag thin films

#### 4.6 Hall Effect Measurements

The Hall effect tested for SnS, SnS: Ag, and Cu-doped SnS: Ag thin films prepared at different Cu ratios by PLD on glass slides. By using of Hall coefficient for each sample the charge carrier ( $n_H$ ) and mobility ( $\mu_H$ ) were calculated using Equation (2.11) and Equation (2.12). Both the SnS and SnS and (SnS: Ag)<sub>0.85</sub>Cu<sub>0.15</sub> were p-type, while the three others are n-type.

The variation of  $n_H$  and  $\mu_H$  for the prepared samples were illustrated in Table 4.7 and Figure 4.11. It was found that the charge carrier concentration increases, with increasing the metal content (Ag and Cu at different ratios) as a result of creating more free charge carriers with the doping process (Hoye *et al.* 2013), while the mobility ( $\mu_H$ ) decreased at 0.05 Cu ratio and increased with more ratio. Such behavior is expected as a result of the opposite variation of particle size with the Cu content. Reducing the crystalline size caused to created more grain boundaries against conducting the charge current (Vladimirov *et al.* 2018). A few factors, including particle size, content, defects, and

surface roughness, affect the conductivity of SnS thin films. The electrical characteristics of the films would alter if these properties changed (Hegde *et al.* 2018). Here, there are two reasons for an increase in the sample conductivity. First, the charge carrier mobility is reduced when crystallite size decreases and localized states are increased with doping.

**Table 4.7** Hall effect coefficients for SnS, SnS: Ag, and Cu-doped SnS: Ag thin films at different Cu ratios prepared by the PLD technique

Sample	Type	n (cm <sup>-3</sup> )	μ <sub>H</sub> (cm <sup>2</sup> /v.sec)	σ <sub>RT</sub> (Ω <sup>-1</sup> .cm <sup>-1</sup> )
SnS	P	1.88E+13	147.00	4.42E-04
SnS:Ag	n	4.98E+13	138.20	1.10E-03
SnS:Ag+0.05 Cu	n	6.40E+13	102.00	1.04E-03
SnS:Ag+0.10 Cu	n	1.06E+15	113.17	1.92E-02
SnS:Ag+0.15 Cu	p	3.79E+15	125.00	7.58E-02

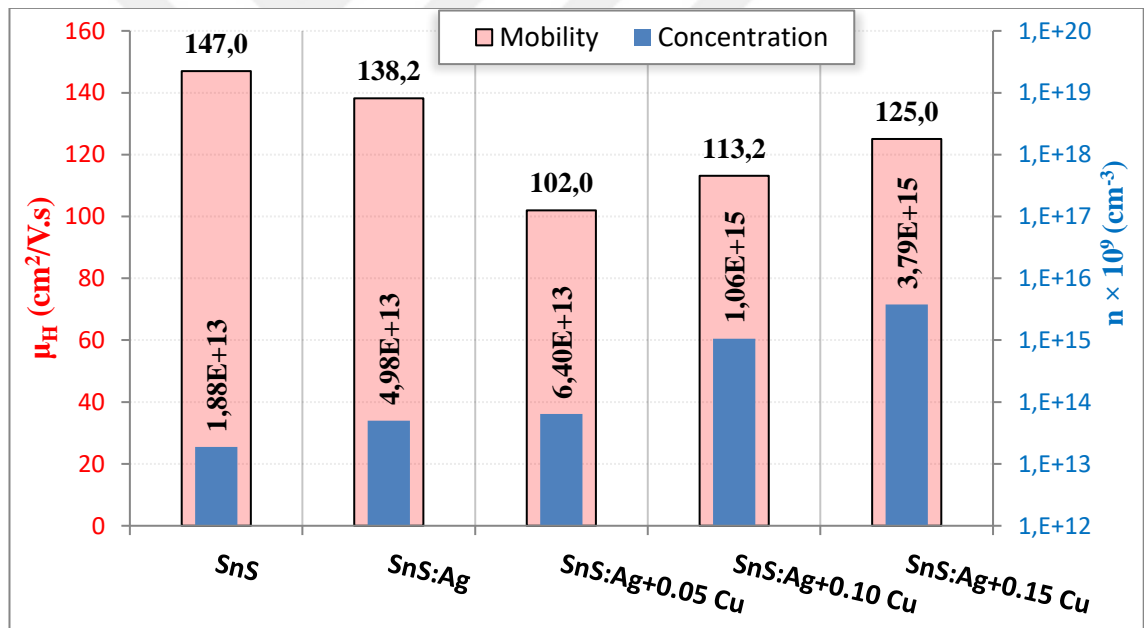


**Figure 4.11** Variation of nH and μH for the SnS, SnS: Ag, and Cu-doped SnS: Ag thin films at different Cu ratios

#### 4.7 I-V Characteristics for Heterojunctions

To determine the behavior of the prepared heterojunctions, current-voltage (I-V) measurements in dark and under illumination were studied. The I-V characteristics for SnS/n-Si, SnS:Ag/p-Si, (SnS:Ag)<sub>0.95</sub>Cu<sub>0.05</sub>/p-Si, (SnS:Ag)<sub>0.9</sub>Cu<sub>0.1</sub>/p-Si, and

(SnS:Ag)<sub>0.85</sub>Cu<sub>0.15</sub>/n-Si heterojunctions in the dark and under illumination using power densities of 100 mW/cm<sup>2</sup> in forward and reverse bias were shown in Figure 4.12. In dark conditions, all curves have the characteristic of diode behavior, where all curves have exponential shapes, pass through the origin, and the forward current is higher than the reverse current, obeying the relation 2.14.

The induced depletion layer between the junction decreases with increasing of the applied forward voltage causing to increase in the current, while reversed bias increases the width of the depletion layer, so the current is reduced. This behavior indicates junction formation. The illuminated sample showed a cross area in the fourth quarter, in addition, increasing the forward current indicates the occurrence of the photovoltaic effect.

The short circuit current ( $I_{sc}$ ) and open circuit voltages ( $V_{oc}$ ) (the cross points with the two axis) were determined. Also, the greatest efficiency that can be obtained is determined by plotting the largest possible rectangular area within the intersection area. Depending on these parameters, the fill factor (FF) and solar cell efficiency ( $\eta$ ) were calculated according to Equation (2.15) and Equation (2.16).

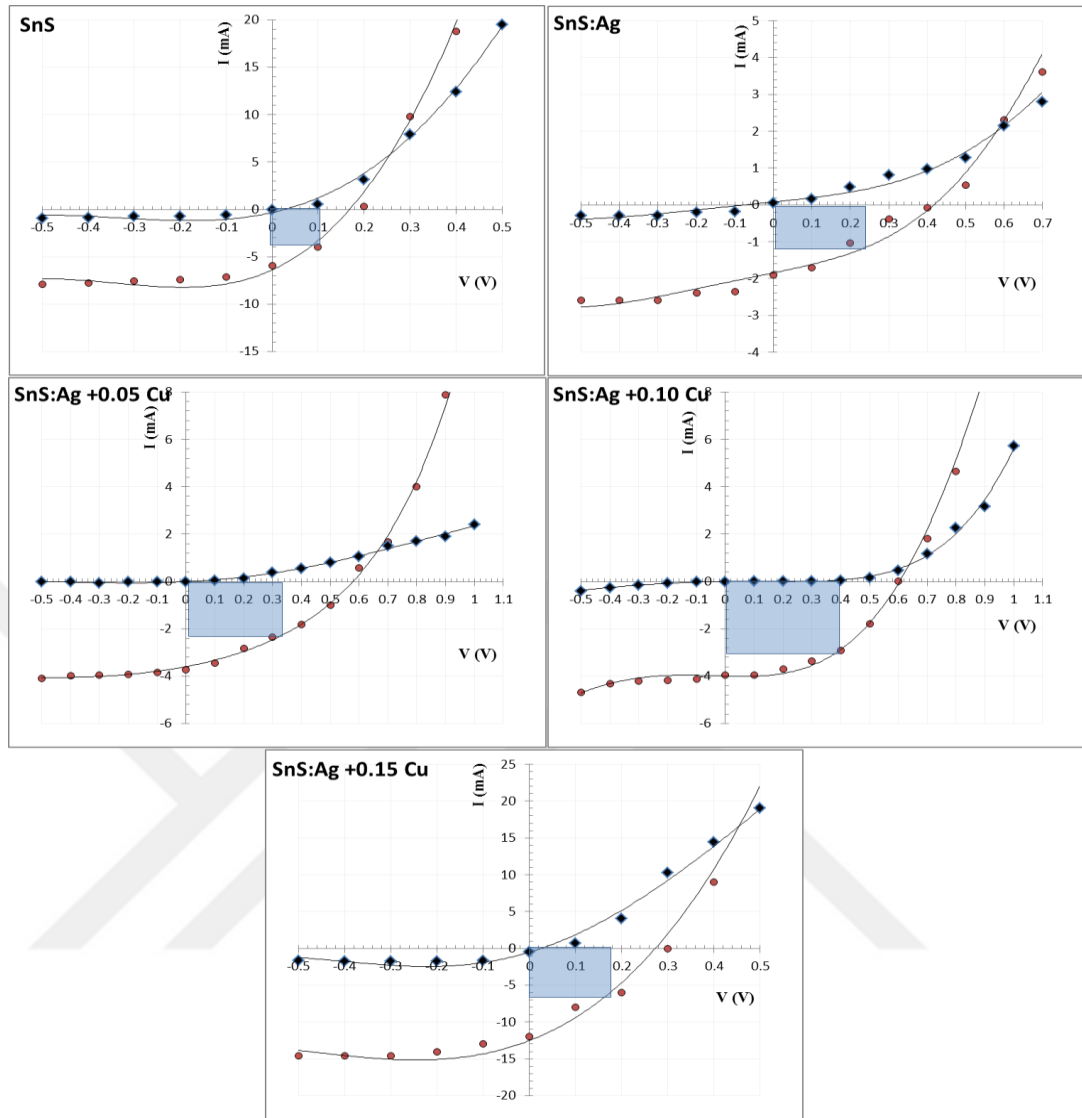


**Figure 4.12** I-V characteristics heterojunctions based on SnS/Si, SnS: Ag/Si, and Cu-doped SnS: Ag/Si thin films at different Cu ratios prepared by PLD

Figure 4.13 shows the relation of  $\ln(I)$  versus forward applied voltage in dark conditions for the prepared heterojunctions. These curves are used to calculate the ideality factor based on Equation (2.14). The non-ideality factor ( $\beta$ ) is calculated from the slope of the liner part from 0 to 0.2 V, which is equal to  $\frac{q}{\beta K_B T}$ , So,  $\beta = 1/(\text{slope} \times 0.0259)$ .

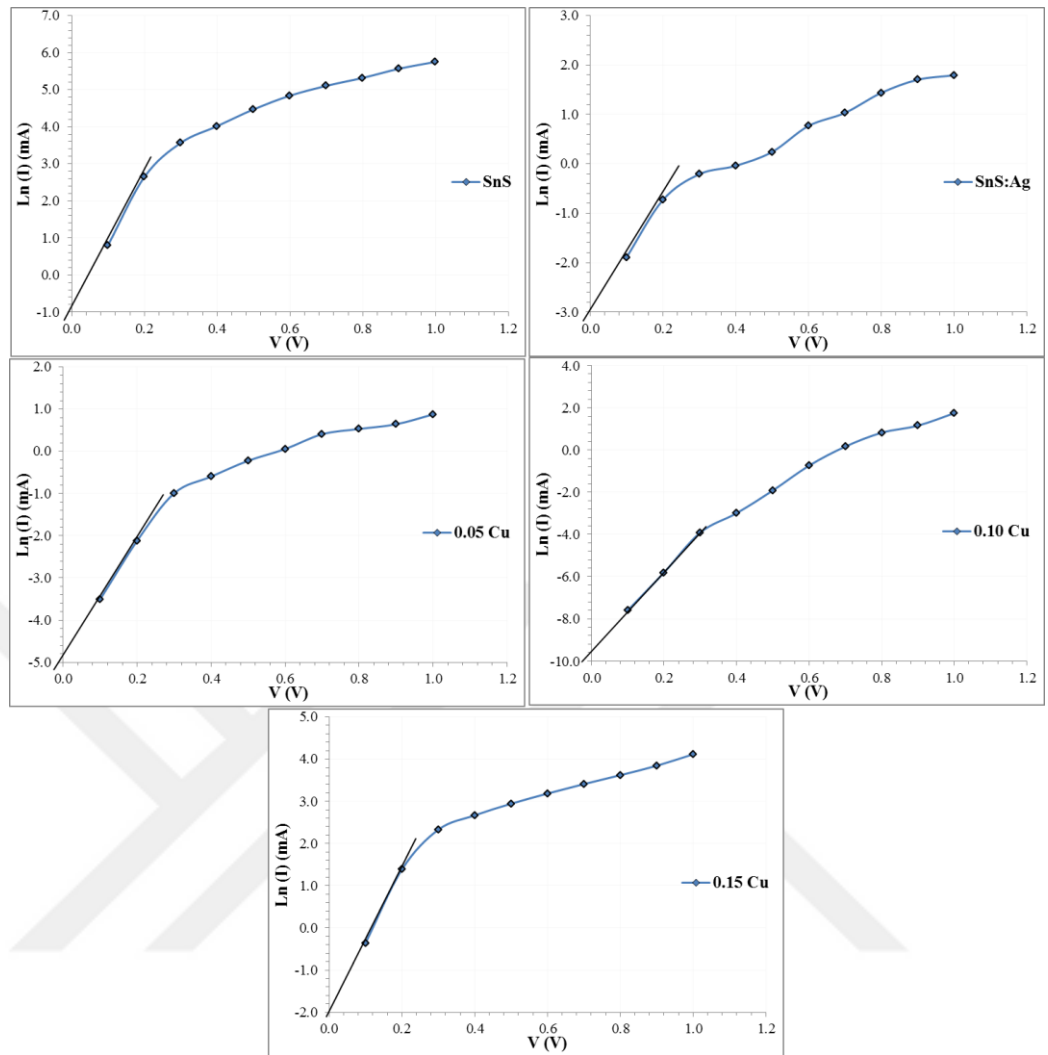


**Figure 4.13**  $\ln(I)$  vs.  $V$  under dark for the heterojunctions based on SnS/Si, SnS: Ag/Si, and Cu-doped SnS: Ag/Si thin films at different Cu ratios

Table 4.8 shows the solar cell parameters for the prepared heterojunctions. It seems that the optimum solar efficiency appeared for the sample  $(\text{SnS:Ag})_{0.9}\text{Cu}_{0.1}/\text{pSi}$ . There is a competition between the transparency (as shown by the UV visible absorbance test) which allow photons to reach the junction, and the sample conductivity where its increment contributes to the conduction of the generated charge carriers and reduces the possibility of recombination, thus contributing to an increase in the circuit current and hence enhance the cell efficiency (Maçaira *et al.* 2015). Therefore, samples with a medium doping ratio (0.1 Cu) have the best efficiency.

There are several researchers that have studied the possibility of improving the efficiency of the heterojunction SnS/Si prepared by several techniques, and the efficiency results were ranging from 0.5 to 2% (Ramakrishna Reddy *et al.* 2010, Minnam Reddy *et al.* 2015). The ideality coefficient values range from 2 to 3.3 and are within the acceptable range.

**Table 4.8** Photovoltaic parameters for the prepared heterojunctions

Sample	I <sub>sc</sub> (mA)	V <sub>oc</sub> (V)	I <sub>m</sub> (mA)	V <sub>m</sub> (V)	FF	Efficiency %	$\beta$
<b>SnS/n-Si</b>	6.00	0.18	4.00	0.10	0.37	0.40	2.09
<b>SnS:Ag/p-Si</b>	2.00	0.40	1.20	0.24	0.36	0.29	3.31
<b>0.05 Cu/p-Si</b>	3.60	0.58	2.40	0.34	0.39	0.82	2.77
<b>0.10 Cu/p-Si</b>	4.00	0.60	3.20	0.40	0.53	1.28	2.15
<b>0.15 Cu/n-Si</b>	12.50	0.28	7.00	0.18	0.36	1.26	2.21

## 5. CONCLUSIONS AND RECOMMENDATION

### 5.1 Conclusions

Studying the characteristics of the SnS, SnS: Ag, Cu-doped SnS: Ag composites thin film at different Cu contents prepared by pulsed laser deposition technique show that it is possible to control the properties of the films prepared by doping at a specific ratio for use in a photovoltaic application, as follows:

The X-ray diffraction test showed the polycrystalline orthorhombic structure of broad lines feature indicated nanocrystalline for all samples. Additional phases corresponding to Ag and Cu appeared at a high ratio. The crystallite size for SnS: Ag thin films reduced from 15.4 to 12.8 nm after doping with 0.05 Cu, then it increased to 14 and 14.7 with an increasing Cu ratio to 0.10 and 0.15, respectively. While the lattice strain has opposite behavior indicates that the main cause of lattice contraction is due to the nano-size effect.

The AFM test showed that the SnS thin film appeared with a high degree of roughness, large particle size, and wide particle size distribution. The 0.05 Cu-doped SnS: Ag is with lower roughness, and the smallest particle diameter is at 0.10 Cu. Increasing the Cu percentage to 0.15 cause to increased in the surface roughness and average particle size.

The FTIR showed the characteristics bands for SnS in all samples in addition to the band of adsorbed gases from ambient. Most bands shifted towards a higher wavenumber after doping with Ag, as well as with Cu incorporated into the SnS matrix.

The absorbance curves at UV-visible appeared as a gradual absorption edge for all samples. The absorbance increases for the SnS: Ag sample compared with the SnS sample, in addition, increasing the Cu content caused more increase in absorption.

A redshift in the band edge with Cu doping appeared. The band gap is equal to 2.2, 2.05, 2.0, 1.8, and 1.75 eV for SnS, SnS:Ag, (SnS:Ag)<sub>0.95</sub>Cu<sub>0.05</sub>, (SnS:Ag)<sub>0.9</sub>Cu<sub>0.1</sub>, and

(SnS:Ag)<sub>0.85</sub>Cu<sub>0.15</sub>, respectively. The direct current conductivity showed two activation energies. These activation energies are reduced by adding Ag and Cu. Both the SnS and (SnS:Ag)<sub>0.85</sub>Cu<sub>0.15</sub> were p-type, while the three others are n-type. The charge carrier concentration increases, with increasing the metal content, while, the mobility has an opposite variation with particle size.

The I-V characteristic showed a typical curve for all samples with an acceptable ideality factor. The illuminated samples show photovoltaic properties of different characteristics. The optimum solar efficiency of 1.28% appeared for the (SnS:Ag)<sub>0.9</sub>Cu<sub>0.1</sub>/pSi heterojunction. This result is comparable to the previous studies for SnS/Si prepared by several techniques. Although, the low efficiency of the obtained heterojunctions, has a low cost of preparation. In addition, it can be used as a photo detector.

## **5.2 Recommendations for Future Work**

- Using different substances as a doping material.
- Using the prepared films in the applications of the optical detectors.
- Testing the prepared samples in gas sensing application.

## REFERENCES

- Abdelrahman, A. E., Yunus, W. M. M. and Arof, A. K. 2012. Optical properties of tin sulphide (SnS) thin film estimated from transmission spectra. *Journal of Non-Crystalline Solids*, 358(12-13): 1447-1451.
- Abegunde, O. O., Akinlabi, E. T., Oladijo, O. P., Akinlabi, S. and Ude, A. U. 2019. Overview of thin film deposition techniques. *AIMS Materials Science*, 6(2): 174-199.
- Adler, D. 1971. Amorphous semiconductors. *Critical Reviews in Solid State and Material Sciences*, 2(3): 317-465.
- Aksay, S., Özer, T. and Zor, M. 2009. Vibrational and X-ray diffraction spectra of SnS film deposited by chemical bath deposition method. *The European Physical Journal-Applied Physics*, 47(3).
- Babar, A. R., Shinde, S. S., Moholkar, A. V., Bhosale, C. H., Kim, J. H. and Rajpure, K. Y. 2011. Physical properties of sprayed antimony doped tin oxide thin films: The role of thickness. *Journal of Semiconductors*, 32(5): 053001.
- Baby, B. H. and Mohan, D. B. 2019. Structural, optical and electrical studies of DC-RF magnetron co-sputtered Cu, In & Ag doped SnS thin films for photovoltaic applications. *Solar Energy*, 194: 61-73.
- Baco, S., Chik, A. and Yassin, F. M. 2012. Study on optical properties of tin oxide thin film at different annealing temperature. *Journal of Science and Technology*, 4(1).
- Barhdadi, A., Hartiti, B. and Muller, J. C. C. 2012. Active defects generated in silicon by laser doping process. *The African Review of Physics*, 6.
- Bird, J. P. 2002. Semiconductors: An introduction. In *Encyclopedia of Materials: Science and Technology*, 1–16.
- Bragg, W. H. and Bragg, W. L. 1915. *X rays and crystal structure*. George Bell & Sons, 229 page, London.
- Caballero-Calero, O., Ares, J. R. and Martín-González, M. 2021. Environmentally friendly thermoelectric materials: High performance from inorganic components with low toxicity and abundance in the earth. *Advanced Sustainable Systems*, 5(11): 2100095.

- Chopra, K. N. and Maini, A. K. 2010. Thin films and their applications in military and civil sectors. Ministry of Defence, 120 page, New Delhi.
- Choy, K. L. 2003. Chemical vapour deposition of coatings. *Progress in Materials Science*, 48(2): 57-170.
- Chrisey, D. B. and Hubler, G. K. 1994. Pulsed laser deposition of thin films. John Wiley & Sons, 613 page, Oxford.
- Dai Nguyen, T., Hung, N. M., Arepalli, V. K., Kim, J., Raj, M. and Nguyen, T. T. O. 2021. Synthesis of Ag-embedded SnS films by the RF method for photovoltaic applications. *Surfaces and Interfaces*, 25: 101151.
- Dar, M. A., Govindarajan, D. and Dar, G. N. 2021. Facile synthesis of SnS nanostructures with different morphologies for supercapacitor and dye-sensitized solar cell applications. *Journal of Materials Science: Materials in Electronics*, 32(15): 20394-20409.
- Dresselhaus, M. S. and Thomas, I. L. 2001. Alternative energy technologies. *Nature*, 414(6861): 332-337.
- Dridi, Z., Bouhafs, B. and Ruterana, P. 2003. First-principles investigation of lattice constants and bowing parameters in wurtzite  $\text{Al}_x\text{Ga}_{1-x}\text{N}$ ,  $\text{In}_x\text{Ga}_{1-x}\text{N}$  and  $\text{In}_x\text{Al}_{1-x}\text{N}$  alloys. *Semiconductor Science and Technology*, 18(9): 850.
- Eason, R. 2006. Pulsed laser deposition of thin films: applications-led growth of functional materials. John Wiley & Sons, 682 page, Oxford.
- Elliott, R. J. and Gibson, A. F. 1975. An introduction to solid state physics and its applications. American Institute of Physics, 490 page, New York.
- Eltawil, M. A., Zhengming, Z. and Yuan, L. 2009. A review of renewable energy technologies integrated with desalination systems. *Renewable and Sustainable Energy Reviews*, 13(9): 2245-2262.
- Farret, F. A. and Simões, M. G. 2006. Integration of alternative sources of energy. Piscataway, NJ, USA: IEEE Press, 50(4).
- Gao, S., Li, W., Dai, J., Wang, Q. and Suo, Z. 2021. Effect of transition metals doping on electronic structure and optical properties of  $\beta\text{-Ga}_2\text{O}_3$ . *Materials Research Express*, 8(2): 025904.
- Greiner, R. A. 1961. Semiconductor devices and applications. McGraw-Hill Book Company, 493 page, New York.

- Greiner, R. A. and Eggers, J. 1989. The spectral amplitude distribution of selected compact discs. *Journal of the Audio Engineering Society*, 37(4): 246-275.
- Hall, E. H. 1879. On a new action of the magnet on electric currents. *American Journal of Mathematics*, 2(3): 287-292.
- Hegde, S. S., Kunjomana, A. G., Murahari, P., Prasad, B. K. and Ramesh, K. 2018. Vacuum annealed tin sulfide (SnS) thin films for solar cell applications. *Surfaces and Interfaces*, 10: 78-84.
- Higler, R. and Sprakel, J. 2017. Doping colloidal bcc crystals—interstitial solids and meta-stable clusters. *Scientific Reports*, 7(1): 1-13.
- Hoye, R. L., Musselman, K. P. and MacManus-Driscoll, J. L. 2013. Research update: Doping ZnO and TiO<sub>2</sub> for solar cells. *APL Materials*, 1(6): 060701.
- Huang, Z., Thomson, P. and Di, S. 2007. Lattice contractions of a nanoparticle due to the surface tension: A model of elasticity. *Journal of Physics and Chemistry of Solids*, 68(4): 530-535.
- Jain, P. and Arun, P. 2013. Parameters influencing the optical properties of SnS thin films. *Journal of Semiconductors*, 34(9): 093004.
- Jiles, D. C. 2014. Electrical and magnetic properties of materials. In *Introduction to the Principles of Materials Evaluation*, 77–96.
- Jose, J., Ravindran, A. and Nair, K. K. 2017. A review on ZnO heterojunction photodetector for UV application. *ICTACT Journal on Microelectronics*, 2: 305-310.
- Joshi, M. P., Khot, K. V., Ghanwat, V. B., Kharade, S. D., Bagade, C. S., Desai, N. D. and Bhosale, P. N. 2018. Synthesis of tin sulphide thin film by simple arrested precipitation technique for solar cell application. In *AIP Conference Proceedings*, AIP Publishing LLC, 1989(1): 2-15.
- Jurablu, S., Farahmandjou, M. and Firoozabadi, T. P. 2015. Sol-gel synthesis of zinc oxide (ZnO) nanoparticles: study of structural and optical properties. *Journal of Sciences, Islamic Republic of Iran*, 26(3): 281-285.
- Kazmerski, L. 1980. *Polycrystalline and amorphous thin films and devices*. Elsevier, 320 page, Amsterdam.

- Kihal, R., Rahal, H., Affoune, A. M. and Ghers, M. 2017. Electrodeposition of SnS thin film solar cells in the presence of sodium citrate. *Journal of Electrochemical Science and Technology*, 8(3): 206-214.
- Kohl, P. A. 1998. Photoelectrochemical etching of semiconductors. *IBM Journal of Research and Development*, 42(5): 629-638.
- Koteeswara Reddy, N., Devika, M. and Gopal, E. S. R. 2015. Review on tin (II) sulfide (SnS) material: synthesis, properties, and applications. *Critical Reviews in Solid State and Materials Sciences*, 40(6): 359-398.
- Krishnan, K. M. 2021. Principles of materials characterization and metrology. Oxford University Press, 880 page, Oxford.
- Kumar, K. S., Manohari, A. G., Dhanapandian, S. and Mahalingam, T. 2014. Physical properties of spray pyrolyzed Ag-doped SnS thin films for opto-electronic applications. *Materials Letters*, 131: 167-170.
- Leach, M., Reddy, K. R., Reddy, M. V., Tan, J. K., Jang, D. Y. and Miles, R. W. 2012. Tin sulphide thin films synthesised using a two step process. *Energy Procedia*, 15: 371-378.
- Li, S. S. 2006. Classification of solids and crystal structure. In *semiconductor physical electronics*. Springer, 250 page, New York.
- Lide, D. R. 2004. *CRC handbook of chemistry and physics*. CRC Press, 85(1).
- Lin, Y. H. 2009. Structure and properties of transparent conductive ZnO films grown by pulsed laser deposition (PLD). PhD. Thesis, University of Birmingham, 61 page, Birmingham.
- Lindberg, O. 1952. Hall effect. *Proceedings of the IRE*, 40(11): 1414-1419.
- Lindholm, F. A., Fossum, J. G. and Burgess, E. L. 1979. Application of the superposition principle to solar-cell analysis. *IEEE Transactions on Electron Devices*, 26(3): 165-171.
- Maçaira, J., Mesquita, I., Andrade, L. and Mendes, A. 2015. Role of temperature in the recombination reaction on dye-sensitized solar cells. *Physical Chemistry Chemical Physics*, 17(35): 22699-22710.
- Masood, K. B., Kumar, P., Malik, M. A. and Singh, J. 2021. A comprehensive tutorial on the pulsed laser deposition technique and developments in the fabrication of low dimensional systems and nanostructures. *Emergent Materials*, 4(3): 737-754.

- Meskers, C. 2021. Metal processes and applications; An overview. In Principles of Metal Refining and Recycling, Oxford University Press, 450-549.
- Moharam, M. M., El Shazly, A. N., Anand, K. V., Rayan, D. E., Mohammed, M. K., Rashad, M. M. and Shalan, A. E. 2021. Semiconductors as effective electrodes for dye sensitized solar cell applications. Topics in Current Chemistry, 379(3): 1-17.
- Mondal, O., Pal, M., Singh, R., Sen, D. and Mazumder, S. 2015. Influence of doping on crystal growth, structure and optical properties of nanocrystalline CaTiO<sub>3</sub>: a case study using small-angle neutron scattering. Journal of Applied Crystallography, 48(3): 836-843.
- Mott, N. F. and Davis, E. A. 2012. Electronic processes in non-crystalline materials. Oxford University Press, 589 page, Oxford.
- Neamen, D. A. 2003. Semiconductor physics and devices: basic principles. McGraw-Hill, 668 page, New York.
- Norton, K., Kunstmann, J., Ping, L., Rakowski, A., Wang, C., Marsden, A. J. and Lewis, D. J. 2019. Synthetic 2-D lead tin sulfide nanosheets with tuneable optoelectronic properties from a potentially scalable reaction pathway. Chemical Science, 10(4): 1035-1045.
- Pavlovic, T. 2019. The sun and photovoltaic technologies. Springer Nature, 416 page, Pune City.
- Perednis, D. and Gauckler, L. J. 2005. Thin film deposition using spray pyrolysis. Journal of Electroceramics, 14(2): 103-111.
- Pileni, M. P. 2006. Nanocrystals forming mesoscopic structures. John Wiley & Sons, 346 page, Oxford.
- Raha, D. and Das, D. 2013. Nanocrystalline silicon thin films prepared by low pressure planar inductively coupled plasma. Applied Surface Science, 276: 249-257.
- Rai, H. C. 1995. Question bank in electrical and electronics engineering. Galgotia Publication Private Limited, 1152 page, New Delhi.
- Rajput, J. K. and Purohit, L. P. 2016. Comparative study of synthesis of CdO-ZnO nanocomposite thin films by different methods: a review. Nanoscience and Technology, 3(1): 1-5.
- Rajput, N. 2015. Methods of preparation of nanoparticles-a review. International Journal of Advances in Engineering & Technology, 7(6): 1806.

- Ramakrishna Reddy, K., Prathap, P. and Miles, R. 2010. Thin films of tin sulphide for application in photovoltaic solar cells. In: Photovoltaics: Developments, Applications and Impact. Energy Science, Engineering and Technology. Nova Science Publishers, New York, pp. 37-62. ISBN 978-1608760220
- Reddy, V. R. M., Gedi, S., Park, C., Miles, R. and KT, R. R. 2015. Development of sulfurized SnS thin film solar cells. *Current Applied Physics*, 15(5), 588-598.
- Rydosz, A. and Szkudlarek, A. 2015. Gas-sensing performance of M-doped CuO-based thin films working at different temperatures upon exposure to propane. *Sensors*, 15(8): 20069-20085.
- Scherrer, P. 1918. *Göttinger nachrichten gesell. Universität Zu Göttingen*, 2: 98.
- Sebastian, S., Kulandaisamy, I., Arulanantham, A. M. S., Valanarasu, S., Kathalingam, A., Shkir, M. and AlFaify, S. 2019. Enhancement in photovoltaic properties of Nd: SnS films prepared by low-cost NSP method. *Rare Metals*, 1-10.
- Shahid, M. U., Deen, K. M., Ahmad, A., Akram, M. A., Aslam, M. and Akhtar, W. 2016. Formation of Al-doped ZnO thin films on glass by sol-gel process and characterization. *Applied Nanoscience*, 6(2): 235-241.
- Shahsavari, A. and Akbari, M. 2018. Potential of solar energy in developing countries for reducing energy-related emissions. *Renewable and Sustainable Energy Reviews*, 90: 275-291.
- Solyman, L., Walsh, D. and Syms, R. R. 2018. *Electrical properties of materials*. Oxford University Press, 514 page, Oxford.
- Srivind, J., Balamurugan, S., Usharani, K., Prabha, D., Suganya, M., Nagarethinam, V. S. and Balu, A. R. 2018. Visible light irradiated photocatalytic and magnetic properties of Fe-doped SnS<sub>2</sub> nanopowders. *Journal of Materials Science: Materials in Electronics*, 29(11): 9016-9024.
- Tebbe, F. N., Wasserman, E., Peet, W. G., Vatvars, A. and Hayman, A. C. 1982. Composition of elemental sulfur in solution: equilibrium of S<sub>6</sub>, S<sub>7</sub> and S<sub>8</sub> at ambient temperatures. *Journal of the American Chemical Society*, 104(18): 4971-4972.
- Tietze, M. L., Burtone, L., Riede, M., Lüsse, B. and Leo, K. 2012. Fermi level shift and doping efficiency in p-doped small molecule organic semiconductors: a

- photoelectron spectroscopy and theoretical study. *Physical Review B*, 86(3): 035320.
- Toda, Y., Hirayama, H., Kuganathan, N., Torrisi, A., Sushko, P. V. and Hosono, H. 2013. Activation and splitting of carbon dioxide on the surface of an inorganic electride material. *Nature Communications*, 4(1): 1-8.
- Umar, A., Akhtar, M. S., Badran, R. I., Abaker, M., Kim, S. H., Al-Hajry, A. and Baskoutas, S. 2013. Electrical properties of solution processed p-SnS nanosheets/n-TiO<sub>2</sub> heterojunction assembly. *Applied Physics Letters*, 103(10): 101602.
- Vikraman, D., Thiagarajan, S., Karuppasamy, K., Sanmugam, A., Choi, J. H., Prasanna, K. and Kim, H. S. 2019. Shape-and size-tunable synthesis of tin sulfide thin films for energy applications by electrodeposition. *Applied Surface Science*, 479: 167-176.
- Vladimirov, I., Kühn, M., Geßner, T., May, F. and Weitz, R. T. 2018. Energy barriers at grain boundaries dominate charge carrier transport in an electron-conductive organic semiconductor. *Scientific Reports*, 8(1): 1-10.
- Wang, Y., Chen, W., Wang, B. and Zheng, Y. 2014. Ultrathin ferroelectric films: growth, characterization, physics and applications. *Materials*, 7(9): 6377-6485.
- Widegren, J. A. and Finke, R. G. 2003. A review of soluble transition-metal nanoclusters as arene hydrogenation catalysts. *Journal of Molecular Catalysis A: Chemical*, 191(2): 187-207.
- Zaien, M., Ahmed, N. M. and Hassan, Z. 2013. Fabrication and characterization of an n-CdO/p-Si Solar Cell by Thermal Evaporation in a Vacuum,". *International Journal of Electrochemical Science*, 8: 6988-6996.
- Zhou, K., Guo, Z., Liu, S. and Lee, J. H. 2015. Current approach in surface plasmons for thin film and wire array solar cell applications. *Materials*, 8(7): 4565-4581.

## **CURRICULUM VITAE**

### **Personal Information**

Name and Surname : Ameira Abdullah Kareim ALMAULA

### **Education**

MSc Çankırı Karatekin University  
Graduate School of Natural and Applied Sciences 2019-Present  
Department of Physics

Undergraduate University of Baghdad  
Collage of Science 1984-1989  
Department of Physics